CCFE
CULHAM CENTRE FOR FUSION ENERGY

UK Atomic Energy Authority

UKAEA-CCFE-PR(19)64

B Chapman, R O Dendy, S C Chapman, L Holland, S
W A Irvine, and B C G Reman

Theory and simulation of ion cyclotron emission from energetic ion populations with a spherical shell distribution in velocity-space

Theory and simulation of ion cyclotron emission from energetic ion populations with a spherical shell distribution in velocity-space

B Chapman, R O Dendy, S C Chapman, L Holland, S W A Irvine, and B C G Reman

This is a preprint of a paper submitted for publication in Plasma Physics and Controlled Fusion

Comparing theory and simulation of ion cyclotron emission from energetic ion populations with spherical shell and ring-beam distributions in velocity-space

B Chapman[1,2], R O Dendy[1,2], S C Chapman[2], L A Holland[2,3], S W A Irvine[2], and B C G Reman[2,4]

[1] CCFE, Culham Science Centre, Abingdon, OX14 3DB, UK

[2] Centre for Fusion, Space and Astrophysics, University of Warwick, Coventry, CV4 7AL, UK

[3] York Plasma Institute, Department of Physics, University of York, YO10 5DQ, UK

[4] Université de Toulouse, Laboratoire Plasma et Conversion d'Energie, 118 route de Narbonne, F-31062 Toulouse cedex 9, France

E-mail: benjamin.chapman@ukaea.uk

September 2019

Abstract. Observations have recently been made of ion cyclotron emission (ICE) that originates from the core plasma in the DIII-D [1, 2] and ASDEX-Upgrade [3, 4] tokamaks. The ICE spectral peaks correspond to the local cyclotron harmonic frequencies of fusion-born ions close to the magnetic axis, in contrast to the hitherto usual spatial localisation of the ICE source to the outer midplane edge in tokamak and stellarator plasmas. Core ICE is temporally transient, and may be caused by the rapid onset and increase of local fusion reactivity. This would give rise to a highly non-Maxwellian population of fusion-born ions near their birth energy. In an idealised future large tokamak deuterium-tritium scenario, this distribution would initially be a thin spherical shell in velocity-space. In present-day medium-to-large tokamaks with deuterium plasmas, such as ASDEX-Upgrade and KSTAR which are not designed to confine fusion-born ions, formation of the ideal shell is pre-empted by prompt loss orbital effects. The idealised shell distribution would be transient; collisional effects acting on longer timescales would drive the fusion-born ions towards a standard slowing-down distribution. For as long as it persists, as pointed out in Ref.[5], the shell might drive the magnetoacoustic cyclotron instability (MCI), which is the excitation process which underlies ICE. Here we present, under core plasma conditions, direct numerical simulations of ICE generation by a spherical shell distribution of fusion-born ions in velocity-space. These energetic minority ions are found to relax collectively in particle-in-cell (PIC) computations which follow their self-consistent gyro-orbit-resolved dynamics, together with that of the majority thermal ions and electrons, under the Maxwell-Lorentz system of equations. We relate the computational outputs, which extend into the nonlinearly saturated regime of the MCI, to the analytical theory of the linear MCI for shell-type energetic ion distributions, and to fully nonlinear simulations of related ring-beam energetic ion distributions relaxing under the MCI. We conclude that in future simulations for ICE interpretation, ring-beam distributions

may provide an acceptable proxy for shell distributions, while using significantly fewer computational particles and still maintaining a satisfactory signal-to-noise ratio.

PACS numbers: 52.35.Hr, 52.35.Qz, 52.55.Fa, 52.55.Tn

Keywords: ion cyclotron emission, magnetoacoustic cyclotron instability, tokamak, numerical simulation, particle in cell, bispectral analysis

1. Introduction

Ion cyclotron emission (ICE) comprises strongly suprathermal radiation, exhibiting narrow spectral peaks at frequencies corresponding to multiple cyclotron harmonics of one or more energetic ion species. ICE is widely observed in magnetic confinement fusion (MCF) plasma configurations, including: all large tokamaks, notably JET [6, 7, 8, 9, 10, 11], TFTR [12], ASDEX-Upgrade [3, 4, 5], DIII-D [1, 2, 13], JT-60U [14, 15, 16], EAST [17], and KSTAR [18, 19]; and two large stellarators LHD [20, 21] and W7-AS [22]. ICE is detected using passive, non-invasive diagnostics, for example wall-mounted antennae or dedicated radio-frequency probes, and is under consideration for use in ITER [23, 24] to monitor fusion-born alpha-particle populations. The narrow spectral peaks of ICE, combined with the mapping from cyclotron frequency to radial location, indicate that ICE is generated by spatially localised plasma processes. The strongly suprathermal nature of ICE suggests that it arises from a collective instability, hence occurs only where there is strong deviation from the Maxwellian in the velocity distribution of the energetic ions that drive it.

For these reasons, analytical and computational studies carried out in a locally uniform approximation have proven successful in capturing the key observed features of ICE. The driving mechanism for ICE is the magnetoacoustic cyclotron instability (MCI). This was originally formulated theoretically in Ref. [25], and further developed for application to ICE measurements for deuterium-tritium plasmas in the early 1990s [26, 27, 28, 29, 30, 31, 32, 33, 34, 35]. The MCI occurs when a minority energetic ion population, whose velocity-space distribution includes an inversion where $\partial f/\partial \mathbf{v} > 0$, enters into cyclotron resonance with a fast Alfvén wave which is supported by the bulk plasma and propagates nearly perpendicular to the background magnetic field. The necessary sharply defined non-Maxwellian feature in velocity space can originate from fusion reactions in the core plasma, neutral beam injection (NBI), or heating due to externally injected waves in the ion cyclotron range of frequencies (ICRF). In general, there will be a link between the spectrum of waves excited by the MCI and the character of the velocity distribution of the energetic ions which drive the waves. Mapping between the measured ICE signal and the theoretical characteristics of the MCI-excited waves is thus essential to interpreting the energetic ion physics underlying ICE observations. For example, recently, linear analysis of the MCI has successfully been applied to ICE

from JT-60U [36], leading on to a detailed study of the characteristics of the energetic ^3He velocity distribution responsible for driving the ICE [37].

Advances in computational physics have enabled first principles investigations of the MCI and ICE. Full gyro-orbit ion dynamics, evolving self-consistently with the electric and magnetic fields under the Maxwell-Lorentz equations, are followed in kinetic particle-in-cell (PIC) computations that typically encompass tens of millions of interacting ions and electrons; see also Appendix B. These can carry the MCI instability into its nonlinear regime, which further assists comparison between simulated and observed ICE spectra [38, 39]. Using the PIC code EPOCH [40], the nonlinear full gyro-orbit characteristics of fusion-born alpha-particle ICE were modelled [41] for plasma parameters relevant to JET edge plasma conditions. These PIC results were reinforced by subsequent PIC-hybrid simulations of the MCI over longer physical time scales, deep into the nonlinear regime of the instability, in which the ions were treated as particles and the electrons as a massless neutralising fluid [38, 42]. The same PIC-hybrid approach provided an explanation for the NBI ICE observed in LHD [43, 44]. Clear links between ICE and the terminal crash phase of the edge localised mode (ELM) [45, 46, 47, 48, 49, 50] cycle were investigated experimentally in the KSTAR tokamak [18, 19], having been noted early on [7]. Using EPOCH PIC computations, these have been explained in terms of the rapidly changing spectral characteristics of the MCI of fusion-born protons caused by the rapidly decreasing local plasma density during the pedestal collapse through multiple ELM filament bursts [39, 51, 52]. ICE driven by NBI deuterons in KSTAR deuterium plasmas has also been interpreted in terms of the MCI using a PIC approach [39]. PIC computations of a stimulated emission counterpart to the MCI under JET-like conditions identified a potential "alpha-particle channelling" scenario, in which an applied wave stimulates the extraction of energy from a minority alpha-particle population to a majority deuteron population [53].

The ICE observations considered in all the simulations described above were localised to the outer midplane edge region of the MCF plasmas. In these cases, drift orbit, local ionisation, and prompt loss effects typically give rise to the highly non-Maxwellian velocity distributions required for ICE excitation by a local energetic ion population via the MCI. For the reasons given in the literature, in this region of the plasma, it is appropriate to represent the minority energetic ions as a drifting ring-beam distribution in velocity space [28, 29, 30]; that is, $f(\mathbf{v}) \sim \delta\left(v_{\parallel} - v_{\parallel 0}\right) \delta\left(v_{\perp} - v_{\perp 0}\right)$ and generalisations thereof. This form of distribution is not so clearly applicable to recent observations of ICE from the core plasma of ASDEX-Upgrade [4, 3] and DIII-D [1, 2, 13]. It appears that some of these ICE signals are due to fusion-born ions, so it is timely to examine the feasibility of these ions driving ICE via the MCI.

As noted in Refs. [54, 55], the onset of a significant level of fusion reactivity as the temperature of the core plasma rises, creates initially a spherically symmetric shell-type distribution of fusion-born ions in velocity space. As time passes, collisional effects will populate the initially hollow sphere within the shell with slowed-down fusion-born ions, so that eventually their velocity distribution is monotonically decreasing. Additionally,

some of the fusion-born ions will be promptly lost from the plasma on microsecond timescales slower than the ion gyro period. Nevertheless, at early times there is a population inversion which approximates the character of a spherical shell. In general, the true velocity distribution on sub-collisional timescales ($\lesssim 100\mu s$) will be somewhere between a ring-beam and a shell. The ring-beam limit has been extensively investigated, initially analytically [28, 29, 30, 31, 32] and subsequently using first principles kinetic codes [38, 41, 42, 51, 52, 39, 44, 56]. The other asymptotic limit, a shell, has hitherto been studies primarily analytically [26, 27].

In this paper we therefore present PIC simulations of ICE driven, via the MCI, by energetic ion populations that have a spherical shell velocity distribution of the form Eq. 2 below. In section 2 we describe our simulation set-up, including details of the two types of non-Maxwellian distribution functions used to represent the minority energetic ions. In section 2 we show the results of fourteen independent PIC simulations of minority energetic ion populations relaxing under the MCI. These compare simulated ICE spectra from ring-beam distributions, typically used in modelling ICE from the plasma edge, and spherical shell distributions, proposed for modelling ICE from the core plasma. From these simulations, we also show how some ICE spectral peaks at minority ion cyclotron harmonics, which are often observed in experiment, can only be explained through nonlinear interactions. We conclude in section 5, and offer some suggestions for future experimental ICE measurements. We emphasise that we are not explicitly simulating plasmas representative of the core of AUG and DIII-D; rather we are examining the feasibility of MCI driven ICE from fusion-born protons which have a spherical shell velocity distribution under conditions which approximate a typical core plasma.

2. Particle-in-cell simulations of ICE spectra

2.1. Computational approach

To simulate the excitation of ICE by fusion-born protons we use the EPOCH particle-in-cell (PIC) code [40] to self-consistently solve the Maxwell-Lorentz system of equations for $\sim 2 \times 10^7$ computational particles; see also Appendix A. Our computational domain spans one periodic spatial dimension and all three velocity dimensions (1D3V), and the code captures the full gyro-orbit particle dynamics of the electrons, background deuterons, and the minority energetic proton population, while self-consistently evolving all three vector components of the electric and magnetic fields. Our approach is to study the collective relaxation of the energetic ion population under this first principles model, and to analyse the spatio-temporal Fourier transforms of the excited fields, which give rise to the simulated ICE spectra. Our simulations are set up in slab geometry, corresponding to the local approximation; they do not incorporate any toroidal effects or eigenmode structure [33, 34, 35, 57, 58, 59, 60, 61, 62, 63, 64]. This absence is expected to have only marginal consequences for modelling the ICE phenomenology

addressed here, given the success of calculations and computations that use the local approximation in explaining recent results from KSTAR [51, 52, 39] and LHD [43, 44], as well as the ICE observations from JET and TFTR [6, 7, 9, 8, 12, 41, 38].

The core ICE observations that motivate the present study are from deuterium plasmas [1, 2, 3, 4], in which 3.02MeV fusion-born protons are the most energetic minority species. Our PIC simulations therefore focus on the fast relaxation of this population on cyclotron timescales, dependant on its initial distribution in velocity space. These simulations address fourteen plasmas whose parameters are close to those used in the calculation of the linear MCI growth rates in Ref. [27], which are relevant to large or medium-size tokamak plasmas. All the simulations use an initially uniform electron number density $n_e = 1.0 \times 10^{19}\mathrm{m}^{-3}$, and a background magnetic field $B_z = 3.1\mathrm{T}$ oriented perpendicular to the spatial domain. This density is approximately a factor four lower than the densities of typical AUG and DIII-D plasmas, but has been chosen to increase the ratio $v_\perp/v_A$ to ~ 0.77, as distinct from the ~ 0.38 which would apply for a plasma with the same magnetic field and $n_e = 1.0 \times 10^{19}\mathrm{m}^{-3}$. It has been shown that having $v_\perp/v_A \sim 1$ maximises the MCI drive [38, 41, 42, 43, 44], thereby precipitating the excitation of the MCI in a feasible amount of computational time whilst maintaining high signal-to-noise ratios. This is necessary given the large computational resource required for these fourteen fully kinetic nonlinear PIC simulations. In addition, choosing $n_e = 1.0 \times 10^{19}\mathrm{m}^{-3}$ allows closer alignment with the original analytical work of Ref. [27]. The temperatures of the initially Maxwellian background thermal deuterons and electrons are set to 1keV. The bulk deuteron and minority proton number densities are denoted by n_D and n_p respectively, and the fast ion concentration $\xi = n_p/n_D = 10^{-3}$ in all simulations. Such a large concentration is not realistic in tokamak plasmas, but is necessary to obtain adequate signal-to-noise ratios in a feasible amount of computational time. We are confident that the underlying physics remains unchanged, because in earlier computational studies [42], the simulated ICE power was found to scale linearly with fast particle concentration ξ.

In seven of our simulations, the velocity-space distribution of the energetic protons is initialised as a ring-beam distribution with finite thickness in the perpendicular direction:

$$f\left(v_\parallel, v_\perp\right) \propto \exp\left(\frac{-\left(v_\perp - v_{0\perp}\right)^2}{v_{T\perp}^2}\right) \delta\left(v_\parallel\right). \tag{1}$$

Here, $v_\perp$ and $v_\parallel$ are the magnitudes of the velocity components perpendicular and parallel to the magnetic field. The magnitude of the initial perpendicular velocity, and its spread, are denoted by $v_{0\perp}$ and $v_{T\perp}$ respectively. We set the value of $v_{0\perp}$ to correspond to the 3.02MeV birth energy of protons produced in D-D fusion reactions. Across these seven simulations, the value of $v_{T\perp}$ rises from zero to $0.3v_{0\perp}$ in steps of $0.05v_{0\perp}$. It is helpful for benchmarking that the distribution function Eq. 1 for $v_{T\perp} = 0$ reduces to the delta-function form used in previous PIC and hybrid simulations of the MCI [38, 41, 51, 52, 39, 42].

In our second set of seven simulations, we initialise the velocity-space distribution of fusion-born protons as a spherically symmetric shell distribution with finite thickness:

$$f\left(v\right) \propto \exp\left(\frac{-\left(v-v_0\right)^2}{v_T^2}\right). \tag{2}$$

Here v is the magnitude of the velocity vector, v_0 defines the centre of the shell, and v_T is the velocity spread, governing the thickness of the shell in velocity space. We set the value of v_0 to correspond to the 3.02MeV birth energy of the protons, and we increase the value of v_T from 0 to $0.3v_0$ in steps of $0.05v_0$ across the seven simulations. Our approach of comparing the outputs of simulations initialised with Eqs. 1 and 2 enables us to establish how far results for the spherical shell, relevant to the core plasma ICE, deviate from broadly equivalent results from the ring-beam, relevant to edge ICE.

Most of the figures in the following sections omit the results of simulations with $v_T = 0.05v_0$ and $v_{T\perp} = 0.05v_{0\perp}$, because these are very similar to simulations with $v_T = 0.1v_0$ and $v_{T\perp} = 0.1v_{0\perp}$ respectively. These results are, however, shown in Figures which plot growth rates, to enable uniform interpolation between the results of different simulations. Each of the seven ring-beam simulations lasts 40 proton gyroperiods $\tau_{cp} = 2\pi/\omega_{cp}$, where ω_{cp} is the angular cyclotron frequency of the protons; by this time, the instability is well into its nonlinear saturated regime. The seven spherical shell simulations have varying durations, from $70\tau_{cp}$ to $130\tau_{cp}$, depending on the time taken for the instability to reach saturation.

2.2. Energy flow and spectral properties

Let us first examine the evolution of the energies of the fields and particles in our simulations. Figure 1 displays the change in energy density as a function of time for six MCI simulations initialised with a ring-beam velocity distribution, Eq. 1, for the minority protons. The perpendicular velocity spread $v_{T\perp}$, expressed as a fraction of the initial perpendicular velocity $v_{0\perp}$, is shown at the top of each panel. The energy transfer between particles and fields qualitatively resembles that of previous work [38, 41, 39] in which $v_{T\perp} = 0$, with the minority protons transferring their energy to the bulk plasma and to the fields. The duration of the linear phase of the instability, normalised to τ_{cp}, is almost four times longer than in previous simulations. This is consistent with the numerical analytical growth rates that we calculate using a first principles kinetic dispersion solver (see Fig. 7, discussed later) for the present simulation parameters, which are of the order $\sim 10^{-2}\omega_{cp}$, much lower than in previous simulations [38, 41]. Figure 1 shows that the simulation with no perpendicular velocity spread $v_{T\perp}$ reaches saturation earliest, at around $25\tau_{cp}$. As $v_{T\perp}$ is increased, the linear phase of the instability saturates at a later time. The amount of energy transferred from the minority energetic proton population to the fields and bulk plasma is greatest for the case $v_{T\perp} = 0.1v_{0\perp}$ and declines monotonically with $v_{T\perp}$ for $v_{T\perp} > 0.1v_{0\perp}$. Increasing $v_{T\perp}$ affects both the field components in the same way; the peak changes in E_x and B_z energy densities are

approximately five times less in the $v_{T\perp} = 0.3v_{0\perp}$ simulation than in the $v_{T\perp} = 0.1v_{0\perp}$ simulation. In all panels, a nonlinear re-energisation stage begins shortly after saturation and persists for the remainder of the simulation. This stage corresponds to the transit time magnetic pumping phase identified in Ref. [38]. It is least pronounced for the $v_{T\perp} = 0.0$ simulation, and most pronounced for the $v_{T\perp} = 0.1v_{0\perp}$ case, lasting for a smaller fraction of the fixed total simulation time as $v_{T\perp}$ increases further.

Figure 2 shows the corresponding six plots for simulations in which the minority protons are initialised with a spherical shell distribution, Eq. 2. The amount of energy transfer from the minority energetic ions at saturation, shown in all panels of Fig. 2, is more than ten times less than that of their ring-beam counterparts. In all cases, the time taken to reach saturation is at least double that in the ring-beam simulations. The top three panels are qualitatively the same as their ring-beam counterparts; these provide the first confirmation from direct numerical simulation of the earlier analytical result [27] that ICE can be excited via the MCI given an initial spherical shell distribution of minority energetic ions. All three panels show a distinct saturation phase, followed by re-energisation, the amount of which decreases substantially as the velocity spread v_T increases. The bottom three panels differ from the top three and from Fig. 1, in that they do not enter a re-energisation stage after saturation of the MCI. Instead, the magnetic field amplitude saturates at about $t = 80\tau_{cp}$ in all cases. Thereafter the minority protons transfer their energy primarily to the bulk plasma deuterons, while the excited field energy remains approximately constant or declines. This aspect of the nonlinear regime of the MCI would require further study, as a means to transfer energy from fusion-born or NBI ions directly to other ion species on cyclotron timescales [65].

An advantage of the long duration of both sets of simulations is that this enables very high frequency resolution when performing Fourier transforms, and these demonstrate further that in all cases the instability is the MCI. Figure 3 shows, for the ring-beam simulations, the distribution of energy in the z-component of the magnetic field in frequency-wavenumber space, where the Fourier transform is performed over the entire time duration and the full spatial domain of the simulations. Each panel is plotted using the same $\log_{10}$ scale, and the fast Alfvén wave branch deviates increasingly from a straight line as ω rises towards the lower hybrid frequency.

Each panel shows a series of well defined resonances along the magnetoacoustic-fast Alfvén branch at sequential integer multiples of ω_{cp}. These resonances are strongest for the simulations with little or no perpendicular spread $v_{T\perp}$. This is consistent with Fig. 1, which shows these simulations have the greatest energy transfer from the minority protons to the excited magnetic field oscillations. In addition to the resonances along the magnetoacoustic-fast Alfvén branch, we see regions of high spectral density at $\omega = 7\omega_{cp}$ and $\omega = 8\omega_{cp}$ at lower wavenumber. The intensity of these regions decreases as $v_{T\perp}$ increases. These additional modes are nonlinear in origin, and arise because of intense phase coupling between modes on the main magnetoacoustic branch, which we will address later in this section. Meanwhile we note that these modes have similar intensity

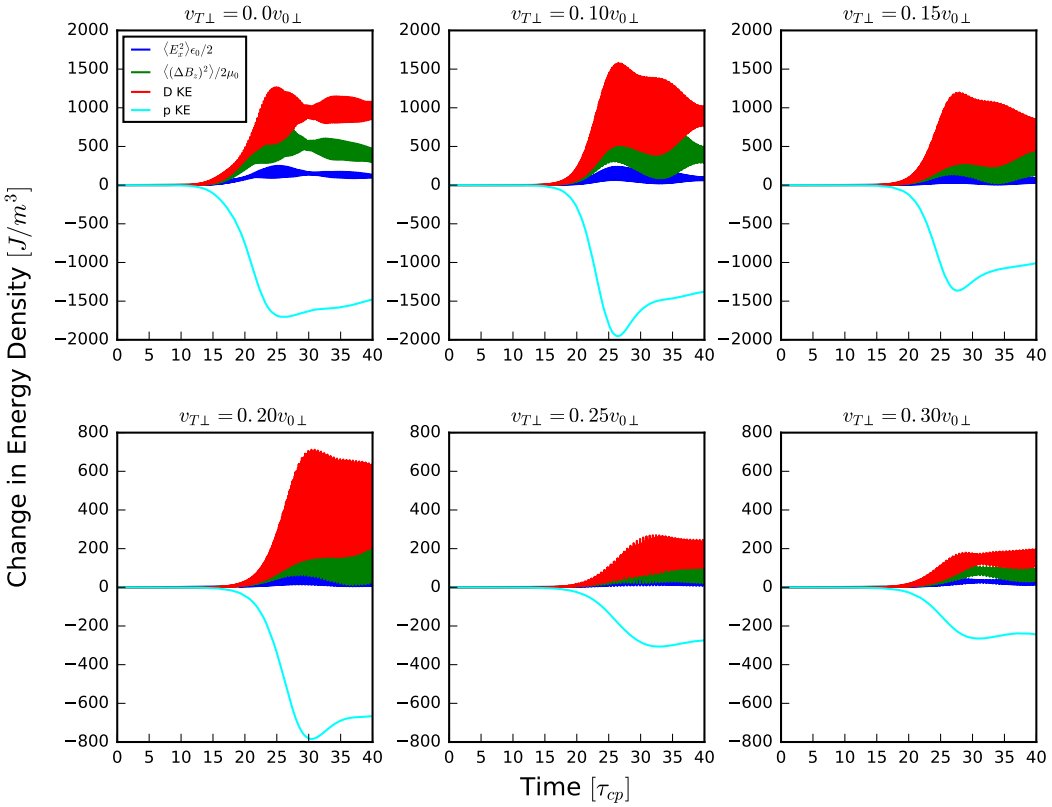

Figure 1: Time evolution of the change in energy density of particles and electric and magnetic field components, from six PIC simulations in which the minority energetic protons are initialised with ring-beam velocity distributions that have different perpendicular velocity spreads $v_{T\perp}$. The value of $v_{T\perp}$ as a fraction of the initial perpendicular velocity $v_{0\perp}$ is shown at the top of each panel. The traces, ordered from top to bottom at their peak (and in colour online) are: Top (red) the change in kinetic energy density of the thermal bulk plasma deuterons; second (green) the energy density of the magnetic field perturbation ΔB_z; third (blue) the energy density of the electrostatic field E_x; fourth (cyan) the change in kinetic energy density of the minority energetic protons. Time is normalised to the proton gyro-period. Note the different y-axis scales on the top and bottom rows. Note the apparent thickness of some traces reflects the envelope of the frequency oscillations of the fluctuating quantities they represent.

to their linearly excited counterparts, suggesting that any ICE spectral peaks at these high frequencies are due, at least in part, to strong nonlinear wave coupling.

The power spectrum for these ring-beam simulations is shown in Fig. 4. There is a strong mode at $\omega = 4\omega_{cp}$ in all panels except for the case $v_{T\perp} = 0.3v_{0\perp}$. At low values of $v_{T\perp}$, there is only a very weak mode at $\omega = 5\omega_{cp}$, which becomes more powerful as $v_{T\perp}$ increases, in conjunction with a decrease in the amplitude of a mode at $\omega = 4\omega_{cp}$.

The corresponding spatio temporal Fourier transform and power spectrum plots

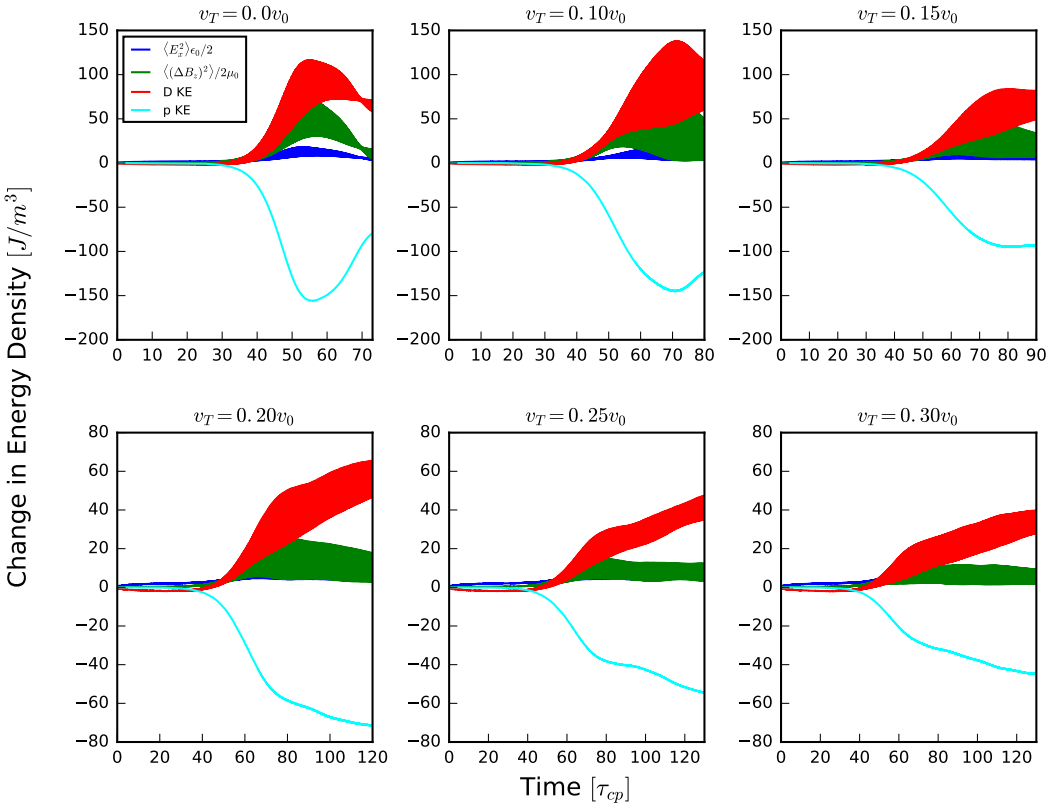

Figure 2: Time evolution of the change in energy density of particles and electric and magnetic field components from six PIC simulations in which the minority energetic protons are initialised with spherical shell velocity distributions that have different velocity spreads v_T. The value of v_T as a fraction of the central velocity v_0 is shown at the top of each panel. The physical meaning of each trace is the same as in Fig. 1. Note the different x-axis and y-axis scales on the top and bottom rows.

for the spherical shell distribution simulations are shown in Figs. 5 and 6 respectively. The frequency resolution of these plots is much greater than that of their ring beam counterparts, owing to the longer simulation durations, up $120\tau_{cp}$ for $v_T \geq 0.2v_0$. Paradoxically this renders it more difficult to pick out the strong, highly localised resonances in the dispersion relation. Due to the longer duration of the shell distribution simulations, there are more data points between adjacent harmonics in Fig. 6 than there are in Fig. 4. Figure 6 therefore appears to have higher noise levels than Fig. 4, but this is not the case; each simulation set has similar noise levels.

In Fig. 5, the $v_T = 0$ simulation shows a faint mode at $\omega = 8\omega_{cp}$ to the left of the main dispersion branch, just as in its ring-beam counterpart panel in Fig. 3. In Fig. 6, the spectral structure is slightly different from that of the ring-beam simulations shown in Fig. 4. The small spectral peaks seen at $\omega = \omega_{cp}$ and $\omega = 2\omega_{cp}$ in Fig. 4 are not present in Fig. 6, and the spectral peak at $\omega = 4\omega_{cp}$ is dominant for the the

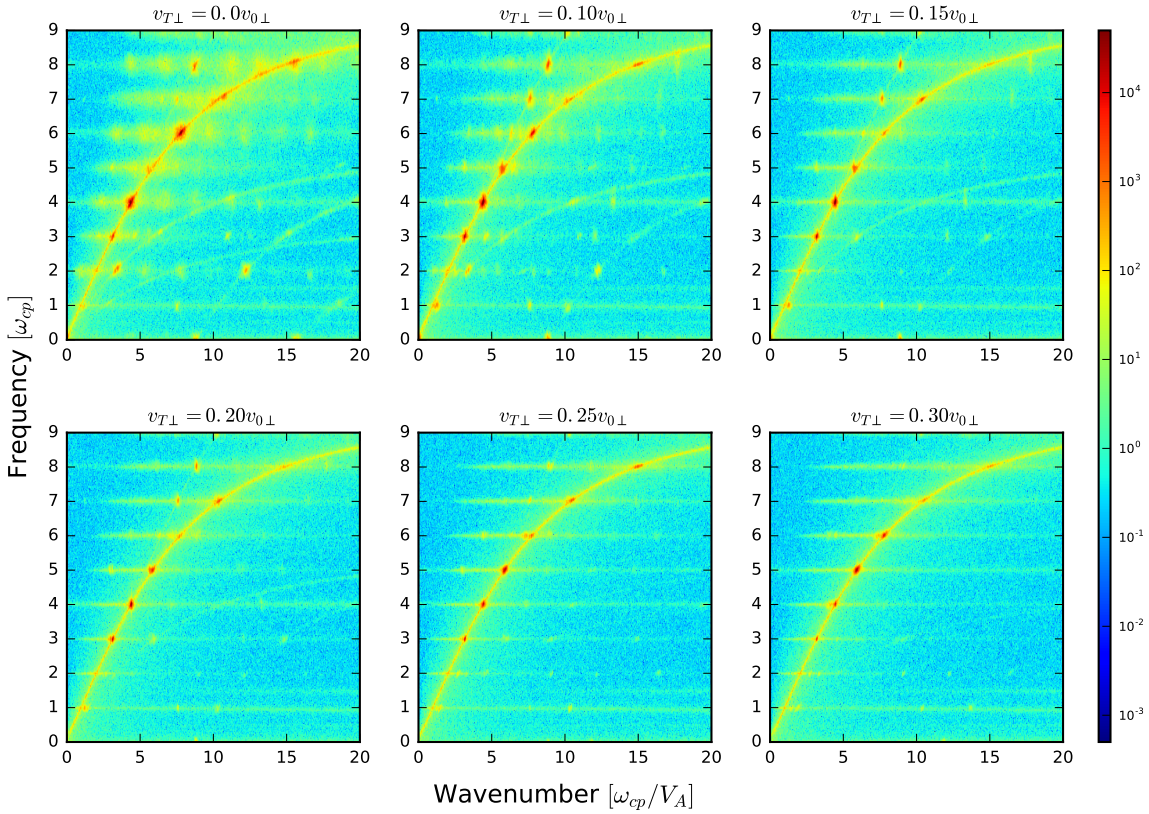

Figure 3: Spectral density of the fluctuating z-component of the magnetic field ΔB_z across frequency-wavenumber space from six PIC simulations in which the minority energetic protons are initialised with ring-beam velocity distributions that have different perpendicular velocity spreads $v_{T\perp}$. The value of $v_{T\perp}$ as a fraction of the initial perpendicular velocity $v_{0\perp}$ is shown at the top of each panel. Each plot is a spatio-temporal Fourier transform of ΔB_z, and spans the entire spatial domain and duration shown in its Fig. 1 counterpart. The colour bar indicates the $\log_{10}$ of the spectral density. Vertical axes are normalised to the minority proton cyclotron frequency ω_{cp}, and horizontal axes to ω_{cp} divided by the Alfvén speed V_A.

simulations with low or zero v_T. In contrast to the ring-beam case shown in Fig. 4, there is no spectral gap at $\omega = 5\omega_{cp}$ in these shell simulations. For $v_T \geq 0.2v_0$, all cyclotron harmonic spectral peaks are roughly equal in magnitude. As v_T increases further, the dominant peak shifts to $\omega = 6\omega_{cp}$, much like the upward shift of the dominant mode in the ring-beam simulations to $\omega = 5\omega_{cp}$. Unlike the ring-beam simulations, the spectral peaks at $\omega = 7\omega_{cp}$ and $\omega = 8\omega_{cp}$ are close in magnitude to the intense peaks at lower frequencies, notably to $\omega = 3\omega_{cp}$.

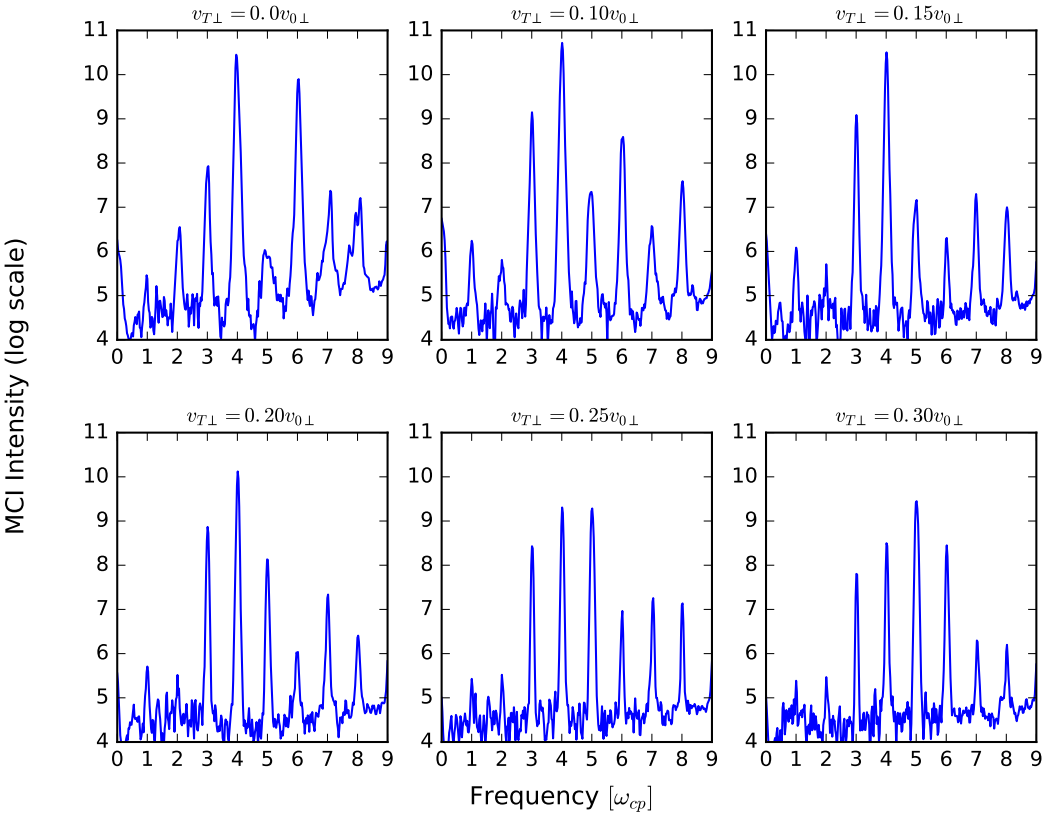

Figure 4: Spectral intensity of the fluctuating ΔB_z field energy density, from six PIC simulations in which the minority energetic protons are initialised with ring-beam velocity distributions that have different perpendicular velocity spreads $v_{T\perp}$. Each panel is constructed by integrating the spatio-temporal Fourier transform in the corresponding panel in Fig. 3 over wavenumber. The value of $v_{T\perp}$ as a fraction of the initial perpendicular velocity $v_{0\perp}$ is shown at the top of each panel. Vertical axes are plotted on a $\log_{10}$ scale, and the horizontal axes are normalised to the minority proton cyclotron frequency ω_{cp}.

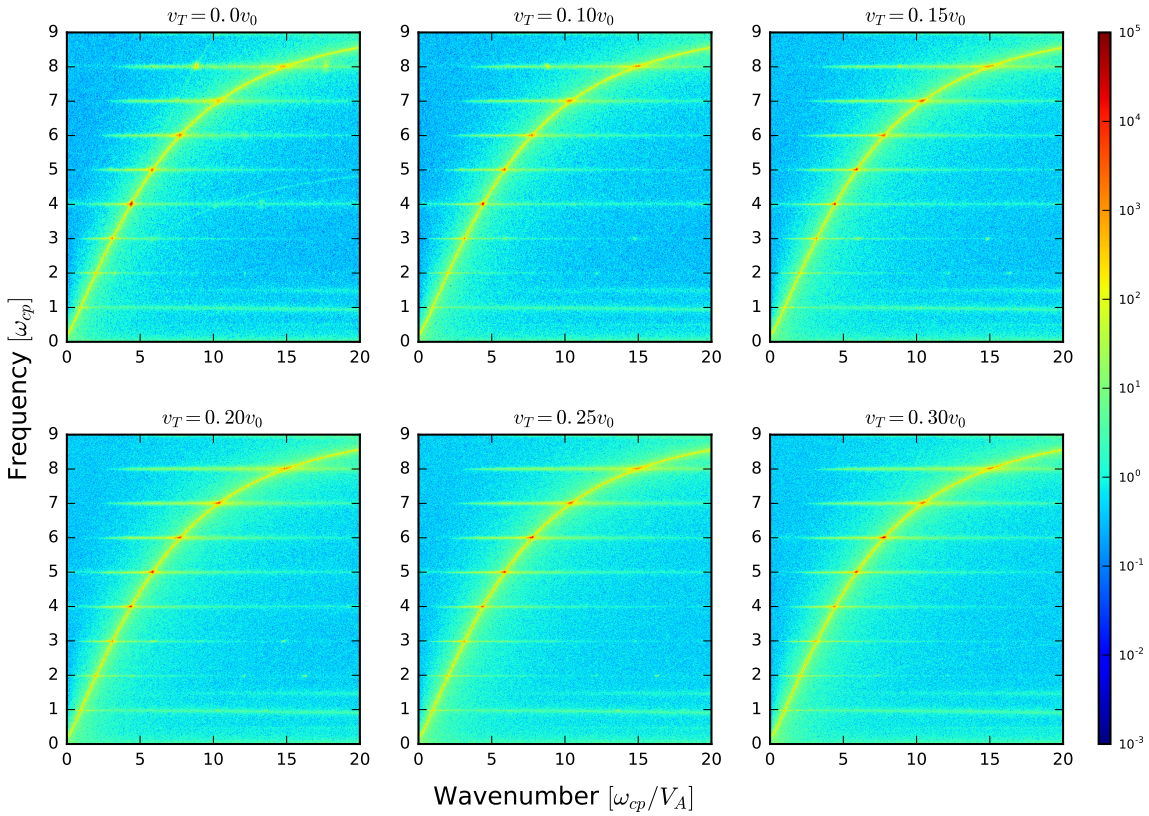

Figure 5: Spectral density of the fluctuating z-component of the magnetic field ΔB_z across frequency-wavenumber space from six PIC simulations in which the minority energetic protons are initialised with spherical shell velocity distributions that have different velocity spreads v_T. The value of v_T as a fraction of the central velocity v_0 is shown at the top of each panel. Each plot is a spatio-temporal Fourier transform of ΔB_z, and spans the entire spatial domain and duration shown in its Fig. 2 counterpart. The colour bar indicates the $\log_{10}$ of the spectral density. Vertical axes are normalised to the minority proton cyclotron frequency ω_{cp}, and horizontal axes to ω_{cp} divided by the Alfvén speed V_A.

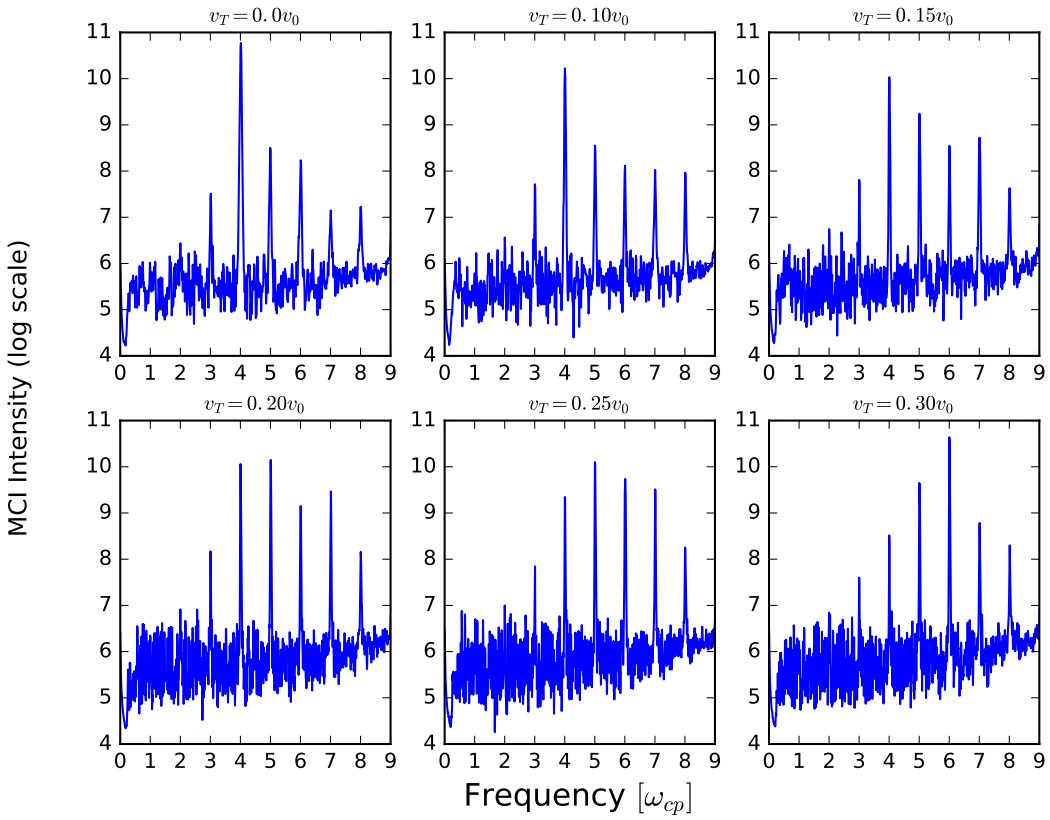

Figure 6: Spectral intensity of the fluctuating ΔB_z field energy density, from six PIC simulations in which the minority energetic protons are initialised with spherical shell velocity distributions that have different perpendicular velocity spreads v_T. Each panel is constructed by integrating the spatio temporal Fourier transform in the corresponding panel in Fig. 5 over wavenumber. The value of v_T as a fraction of the central velocity v_0 is shown at the top of each panel. Vertical axes are plotted on a $\log_{10}$ scale, and the horizontal axes are normalised to the minority proton cyclotron frequency ω_{cp}.

3. Simulation growth rates at early times compared to linear MCI theory

The growth rates of modes at early times can be inferred from both sets of PIC simulations, and are plotted as a function of cyclotron harmonic number and thermal spread in the right panels of Fig. 7. It is helpful to compare these plots to the left panels, which display the numerically computed analytical linear growth rates for the MCI. These are computed numerically using the first principles kinetic dispersion solver [66, 67] outlined in Appendix B. The upper panels of Fig. 7 correspond to a spherical shell distribution, and the growth rates are plotted as a function of the shell spread v_T, while the lower panels correspond to a ring-beam distribution, and are plotted as a function of the perpendicular velocity spread $v_{T\perp}$. To obtain uniform spacing of the data points, two additional PIC simulations were run, corresponding to $v_T = 0.05v_0$ for a spherical shell distribution and $v_{T\perp} = 0.05v_0$ for a ring-beam. These two simulations are not shown in the other figures of this paper, and do not alter any conclusions drawn. In all panels the growth rates are normalised to the proton cyclotron frequency ω_{cp}. The eighth harmonic is not displayed because its numerical analytical linear and PIC-inferred growth rates are zero or negligible in all cases; this mode is almost entirely driven by nonlinear interactions, as we will show later.

The ring-beam growth rates computed from the PIC simulations closely resemble their numerically computed counterparts. For example, the absence of the fifth harmonic in PIC simulations with $v_{T\perp} \leq 0.1$ is replicated by the numerical growth rate solver. The growth of the sixth harmonic at low values of $v_{T\perp}$ is also consistent, as is the tendency for the power to shift from the fourth harmonic to the fifth as $v_{T\perp}$ increases. The magnitudes of the growth rates differ slightly, with the maximum value inferred from the simulation being ~ 1.7 times larger than the maximum numerically calculated analytical value. We view this as a reassuring outcome, given the finite signal-to-noise ratio in the simulations. The spherical shell distribution growth rates are similarly consistent, and agree more closely in magnitude. Both PIC simulation and numerically computed analytical growth rates indicate that the growth is concentrated around the fourth proton cyclotron harmonic at low values of v_T, and shifts towards the sixth harmonic as v_T increases. The numerical solver calculates that the fourth and fifth harmonic modes have growth rates which are similar in magnitude, which is not borne out by the simulation results. The solver also predicts that the largest growth rate for $v_T = 0.3v_0$ occurs at the fourth harmonic, while it is the sixth harmonic in the simulations. The overall similarity between numerical analytical and simulation growth rates across fourteen simulations that employ two different energetic proton velocity distributions is encouraging. It reinforces the conclusion that the MCI arises spontaneously in our first principles Maxwell-Lorentz PIC computations.

We have also calculated the linear growth rates for the initial spherical shell distribution using Eq. 31 of Ref. [27], leading to the results shown in Appendix C. This analytical expression predicts the same trend in the magnitude of the growth rate as a function of v_T as in the PIC simulations and numerical solver. However the

peak growth rate is located at the sixth harmonic as opposed to the fourth. As noted in Appendix C, this discrepancy probably arises from the requirement to set the real frequency exactly equal to $k_\perp v_A$ in the linear theory of Ref. [27]. As the frequency tends towards the lower hybrid frequency, this approximation diverges from the true real frequency inferred from our computations, see Fig. 5. Returning to Fig. 7, we note that the tendency of the fastest growing mode in the simulations to shift from the fourth, to the fifth, and finally to the sixth proton cyclotron harmonic as the velocity spread increases is qualitatively the same in both the ring-beam and spherical shell simulations. The only major difference is the presence of faster growing $\omega = 6\omega_{cp}$ modes in the ring-beam simulations.

4. Nonlinear physics of the simulations

4.1. Field energy in the nonlinear phase of the MCI

The nonlinear aspects of PIC simulations are often central to understanding observed ICE phenomenology: for example, in relation to the excitation of alpha-particle cyclotron harmonics $l \leq 6$ in ICE from JET DT plasma [38, 41], and the "ghost" chirping ICE observed at proton cyclotron harmonics $20\omega_{cp} \leq \omega \leq 35\omega_{cp}$ in KSTAR deuterium plasmas [52]. The time evolution of the energy in the fluctuating part of the z-component of the magnetic field, ΔB_z, as a function of wavenumber is shown in Fig. 8 for two simulations of the MCI. The left panel of Fig. 8 results from the repeated spatial Fourier transforms of the fields excited in a ring-beam simulation with $v_{T\perp} = 0$, while the right panel of Fig. 8 is from a spherical shell simulation with $v_T = 0$. Time is normalised to τ_{cp}, wavevector is normalised to ω_{cp}/V_A, and the colour bar indicates the $\log_{10}$ of the spectral density of ΔB_z. In both panels, the strongest modes are centred around $k \sim 4.35\omega_{cp}/V_A$ and $k \sim 7.8\omega_{cp}/V_A$. These begin growing early, in the linear MCI stage of the simulation, and correspond to the fourth and sixth proton cyclotron harmonics respectively. There is also a strong, linearly unstable mode at $k \sim 5.9\omega_{cp}/V_A$ in the right panel, corresponding to the fifth cyclotron harmonic. This mode also appears in the left panel, but it is weaker and starts to grow at a later time $t \approx 20\tau_{cp}$, well after the linear phase of the MCI. In both panels of Fig. 8, at this later time there also appears a mode at $k \sim 8.7\omega_{cp}/V_A$, which contributes to the eighth proton cyclotron harmonic spectral peak in both simulations. A mode at $k \sim 15.5\omega_{cp}/V_A$ appears only after $t \simeq 20\tau_{cp}$ in the left panel, but is weakly linearly driven in the right panel. Other modes that first appear at $t \simeq 20\tau_{cp}$ can be seen in both panels, more clearly in the left panel.

Figure 9 shows the evolution of B_z^2 as a function of time in the $v_{T\perp} = 0$ ring-beam simulation for: two linearly unstable modes, at $k \simeq 4.35\omega_{cp}/V_A$ and $k \simeq 7.8\omega_{cp}/V_A$; and two modes that first appear after $t \approx 15\tau_{cp}$, at $k \simeq 8.7\omega_{cp}/V_A$ and $k \simeq 15.5\omega_{cp}/V_A$. These traces were obtained by averaging over a narrow range of wavevectors in the vicinity of these modes; there is no overlap with other, clearly distinct, modes shown in

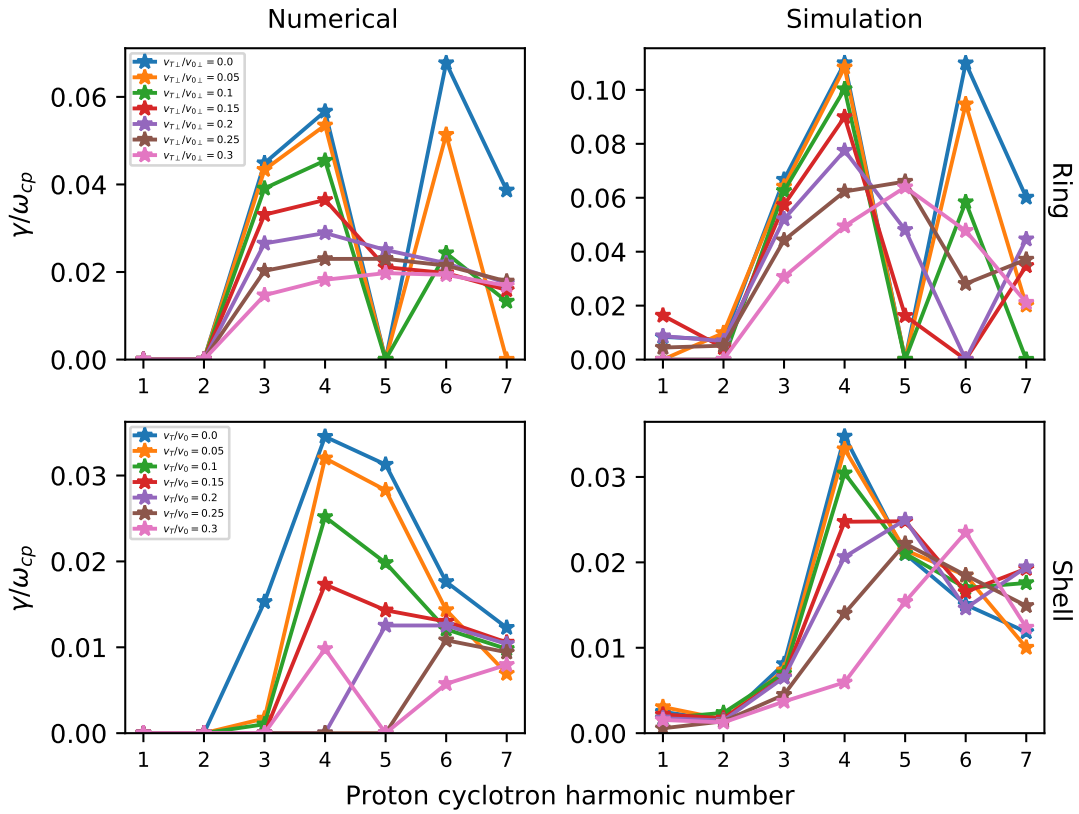

Figure 7: Growth rates of the MCI calculated for different values of velocity spread and plotted as a function of proton cyclotron harmonic number. Coloured stars denote calculated values, coloured lines are a guide to the eye. The magnitude of the growth rate γ is normalised to the proton cyclotron frequency ω_{cp}. Upper panels: Growth rates corresponding to a minority proton ring-beam distribution function with varying perpendicular velocity spread $v_{T\perp}$. Lower panels: Growth rates corresponding to a minority proton spherical shell distribution function with varying velocity spread v_T. Left panels: Linear growth rates calculated numerically from a kinetic dispersion solver, details of which are given in Appendix B. Right panels: Growth rates calculated directly from PIC simulations. In all panels the eighth proton cyclotron harmonic is omitted, because it has a zero or negligible linear growth rate in all cases. In the upper panels, corresponding to the ring-beam distribution, the numerical and PIC growth rates differ slightly in their maximum and minimum values, but the left and right plots are qualitatively almost identical. In the lower panels, corresponding to the spherical shell distribution, the numerical and PIC growth rates have the same maximum and minimum values, but the left and right plots are not as qualitatively similar as their ring-beam counterparts. The corresponding analytical linear growth rates of a minority proton spherical shell distribution relaxing under the MCI have been calculated according to Eq. 31 of Ref. [27], and are shown in Appendix C.

Fig. 8. A moving average was also applied in time, to smooth out the field oscillations. The $k \simeq 8.7\omega_{cp}/V_A$ mode reaches a slightly higher saturation energy, and begins growing slightly later in time than the $k \simeq 15.5\omega_{cp}/V_A$ mode. The upper left panel of Fig. 3 shows that both these modes have a strong resonance at $\omega = 8\omega_{cp}$, along the eighth

proton cyclotron harmonic, and thus both contribute with similar magnitude to the $\omega = 8\omega_{cp}$ peak shown in the top left panel of Fig. 4. The saturation energy of the linearly unstable modes is more than two orders of magnitude greater than that of the nonlinearly driven modes, and is therefore not displayed in Fig. 9.

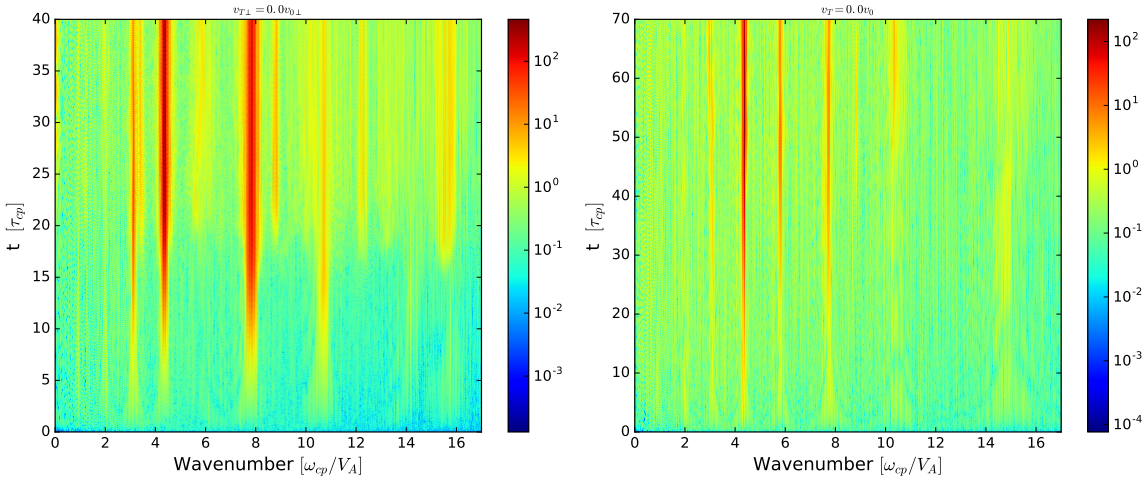

Figure 8: Time evolution of the spectral density of the fluctuating z-component of the magnetic field ΔB_z across wavenumber space. Left: From a PIC simulation in which the minority energetic protons are initialised using a ring-beam velocity distribution with no perpendicular velocity spread; corresponding to the upper left panels of Figs. 1, 3, and 4. Right: From a PIC simulation in which the minority energetic protons are initialised using a spherical shell velocity distribution with no velocity spread; corresponding to the upper left panels of Figs. 2, 5, and 6. The colour bar indicates the $\log_{10}$ of the spectral density of ΔB_z. The vertical axes are normalised to the minority proton gyroperiod $\tau_{cp} = 2\pi/\omega_{cp}$, and extended to $40\tau_{cp}$ (left) and $70\tau_{cp}$ (right). The horizontal axes are normalised to ω_{cp} divided by the Alfvén speed V_A.

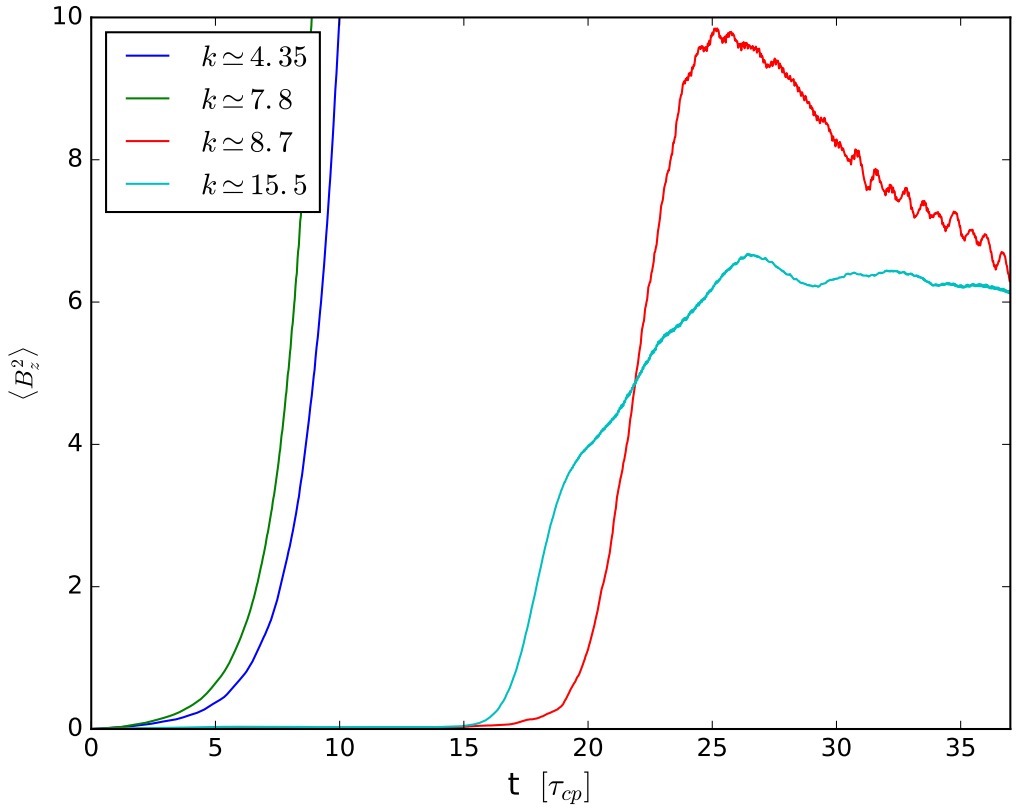

Figure 9: Time evolution of the energy density of the oscillating magnetic field component ΔB_z that is localised in wavenumber space close to values normalised with respect to ω_c/V_A that are indicated in the box in the top left of the figure. These traces are derived from the information displayed in the left panel of panel of Fig. 8, for a PIC simulation in which the minority energetic protons are initialised with a ring-beam distribution that has no perpendicular velocity spread. A moving average has been applied in time, so as to smooth out the field oscillations that are visible in the green trace in the corresponding top left panel of Fig. 1. The two left-most modes are linearly unstable and grow from the start of the simulation. They reach a saturation energy (not shown) around two orders of magnitude higher than that of the two right-most modes, which begin to grow at $t \approx 15\tau_{cp}$, long after the two left-most modes have exponentiated. Thus $t \approx 15\tau_{cp}$ demarcates the start of the nonlinear phase of the simulation, during which the two right-most modes are driven by nonlinear wave interactions, see Section 4.2.

4.2. Bicoherence analysis of nonlinear wave coupling

We now quantify the extent and consequences of nonlinear wave-wave coupling. The best numerical measure of this is obtained from the simulation outputs by bispectral analysis [68, 69, 70, 71, 72] thereof; for a brief account, see Appendix D. The bicoherence b_c, see Eq.(D.2), is bounded between 0 and 1 and measures the fraction of the Fourier power of a signal that is due to nonlinear (specifically, quadratic) interactions between three waves that satisfy the frequency and wavenumber matching criteria: $f_3 = f_1 + f_2$ and $\boldsymbol{k_3} = \boldsymbol{k_1} + \boldsymbol{k_2}$. Bispectral analysis has been successfully applied to ICE data and MCI simulations [38, 52], and to other experimental plasma measurements [73, 74, 75, 50].

The squared bicoherence $b_c^2\,(k_1, k_2)$ is plotted in Fig. 10 for the six MCI simulations previously considered in Figs. 1, 3, and 4, in which the minority protons are initialised with a ring-beam velocity distribution. It is a function of wavenumber, which, for the strongest modes, maps directly to frequency. Shading indicates the intrinsic strength of nonlinear coupling, 1 (dark red) being completely coupled and 0 (dark blue) completely uncoupled. In each plot, b_c^2 is calculated over the full $40\tau_{cp}$ duration of simulation data; the time integration window of each successive Fourier transform is $1.25\tau_{cp}$, and the overlap of successive Fourier transforms is $0.25\tau_{cp}$. The number of independent samples is thus 32, implying a significance level of $b_c^2 \sim 0.177$; as we shall show, this is far lower than the coupling strength of the modes of interest. For brevity, in the following we refer to frequencies by their proton cyclotron harmonic number l, e.g. $\omega = 4\omega_{cp}$ becomes $l = 4$. Similarly for the wavenumbers, e.g. "$k = 4.35$" refers to $k = 4.35\omega_{cp}/V_A$. We shall refer to parent modes using the subscripts 1 and 2, and child modes using the subscript 3, as in Appendix D.

All six panels of Fig. 10 display multiple regions of strong nonlinear wave-wave coupling. In general, the strength of this coupling decreases as $v_{T\perp}$ increases, which is in part due to the shorter duration of the nonlinear re-energisation stage of the simulation. In each panel a mode at $(k_1, l_1) \approx (4.35, 4)$ interacts strongly with all other modes, and the strength of this interaction decreases rapidly with increasing $v_{T\perp}$. This mode interacts strongly with itself, and is the origin of the $(k_3, l_3) \approx (8.7, 8)$ mode; in principle, this mode can also couple to other modes. Figure 10 shows that the strength of coupling between the $(k, l) \approx (8.7, 8)$ mode and other modes drops off rapidly as $v_{T\perp}$ increases beyond $0.1v_{0\perp}$. The strength of the phase coupling between the $(5.9, 5)$ mode and other modes (which can be seen by following vertical and horizontal straight lines from $k_2 = 5.9$) is weak at low $v_{T\perp}$. It greatly increases as $v_{T\perp}$ increases, and this mode becomes linearly unstable, as seen in the top left panel of Fig. 7. The same is true of the $(10.5, 7)$ mode, see Figs. 7 and 4.

We can further characterise of nonlinear interactions in these six ring-beam simulations by examining the summed bicoherence Σb_c^2 as a function of $k_3 = k_1 + k_2$. That is, we sum over all values of $b_c^2\,(k_1, k_2)$ for all combinations of (k_1, k_2) for which

$k = k_3 = k_1 + k_2$, and plot the results as a function of k_3. This is plotted in Fig. 11 for each ring-beam simulation. The vertical axis sums all the squared bicoherence contributions from modes k_1 and k_2 which add vectorially to produce modes with $k_3 = k_1 + k_2$. If a wave $k = k_3$ has a large value of Σb_c^2, then there are usually multiple combinations of k_1 and k_2 with large values of b_c^2 that could contribute to the formation of a wave at k_3, given wave power at k_1 and k_2. In Fig. 11, combinations of k_1 and k_2 such that $b_c^2 < 0.8$ are not included in the sum, meaning only modes with the strongest nonlinear couplings are considered.

Considering, for example, the $v_{T\perp} = 0$ panel of Fig. 11, we see spikes at $k_3 \approx 8.7$, 12.2, 13.1, 15.6, and 18.7. The $k_3 \approx 8.7$ spike is the nonlinearly driven mode which contributes to the $l = 8$ proton cyclotron harmonic, and is present in all panels apart from $v_{T\perp} = 0.3v_{0\perp}$. The large spike at $k_3 \approx 12.2$ corresponds to a mode visible in the left panel of Fig. 8, and its parent modes can be identified as $(k_1, l_1) \approx (7.8, 6)$ and $(k_2, l_2) \approx (4.35, 4)$. Interestingly, this $k_3 \approx 12.2$ mode corresponds to two distinct waves, one at $l_3 = l_1 + l_2 = 6 + 4 = 10$, and the other at $l_3 = l_1 - l_2 = 6 - 4 = 2$, the latter can be seen in the top left panel of Fig. 3. The frequency of the $l_3 = 10$ mode exceeds the lower hybrid frequency $\omega_{LH} \approx 9\omega_{cp}$, and hence lies in a region where the linear dispersion relation implies evanescence [52, 76, 77]. Figure 12 shows that ring-beam simulations with finite $v_{T\perp}$ generate similar nonlinearly driven modes in the evanescent region, whose number decreases as $v_{T\perp}$ increases, reflecting the decreasing strength of nonlinear coupling. Considering the top left panel, only the cyclotron harmonics $l = 10$ and $l = 12$ are above the noise level ~ 4 in our units, which is deduced from Fig. 4. The $l = 10$ peak is more than two orders of magnitude above the noise level, and is of comparable magnitude to the linearly unstable peak at $l = 7$ in the same simulation. This $l = 10$ mode persists in the simulations with $v_{T\perp} > 0$, albeit to a lesser degree.

Finally, we note that the nonlinearly driven $(k_3, l_3) \approx (15.6, 8)$ mode in the $v_{T\perp} = 0$ simulation probably owes its existence to the $(k_1, l_1) \approx (12.2, 10)$ and $(k_2, l_2) \approx (3.4, 2)$ modes ($l_3 = 10 - 2 = 8$), which are themselves nonlinearly driven. The $(k_2, l_2) \approx (3.4, 2)$ mode appears in the top left panel of Fig. 3, and in wavevector space is just distinguishable from the linearly unstable $(k, l) \approx (3.3, 3)$ mode. Looking closely in this region of the left panel of Fig. 8, there is a mode evolving during the nonlinear stage of the simulation which is immediately adjacent to the linearly unstable mode at $(k, l) \approx (3.3, 3)$. This is a clear example of two nonlinearly driven modes interacting with each other to produce a further nonlinearly driven mode which is in the range of frequencies which are more easily detectable in experiment.

The squared bicoherence for six MCI simulations in which the minority protons were initialised with a spherical shell distribution is shown in Fig. 13. The plots in Fig.13 were computed using longer time series than their ring-beam counterparts. This results in a lower minimum significance level for these simulations, $b_c^2 \gtrsim 0.13$. For $v_T \leq 0.2v_0$, the $(k, l) \approx (4.35, 4)$ mode is strongly coupled to other modes in the simulation, with the

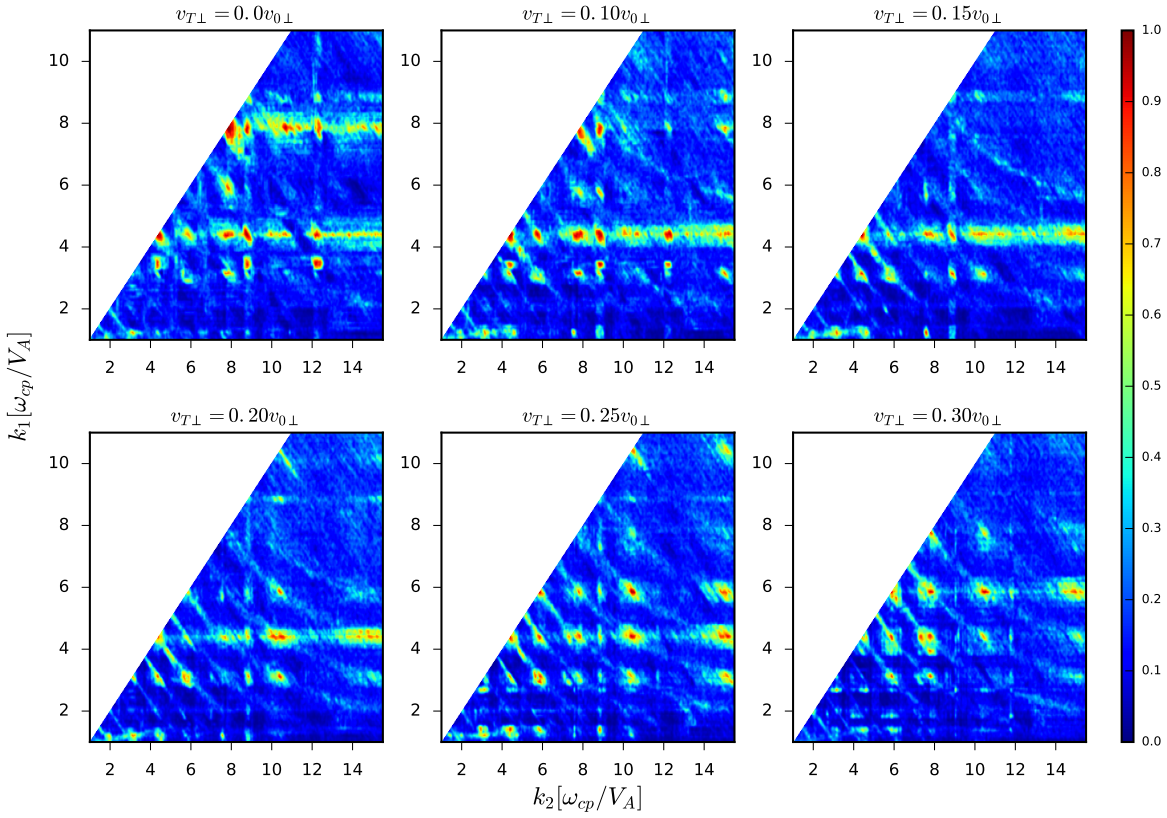

Figure 10: The square of the bicoherence b_c^2 (defined by Eq. D.2) of the oscillatory part of the B_z field component as a function of normalised wavenumber k from six PIC simulations in which the minority energetic protons are initialised using ring-beam velocity distributions with varying perpendicular velocity spreads. The spread $v_{T\perp}$ as a fraction of the initial perpendicular velocity $v_{0\perp}$ is shown at the top of each panel. The colour scale indicates intrinsic nonlinear coupling between waves with wave numbers k_1 and k_2, which takes values between 0 and 1. In each plot, b_c^2 is calculated over the full $40\tau_{cp}$ duration of the simulation; the width of each successive Fourier transform is $1.25\tau_{cp}$; and the overlap of each successive Fourier transform is $0.25\tau_{cp}$. The number of independent samples is thus 32, giving a significance level of $b_c^2 \gtrsim 0.177$.

$v_T = 0$ simulation having by far the weakest (but still statistically significant) coupling. Simulations with $v_T > 0.2v_0$ do not exhibit strong coupling of the $(k, l) \approx (4.35, 4)$ mode, probably because of their characteristically different nonlinear stage, see panels $v_T = 0.25v_0$ and $v_T = 0.3v_0$ of Fig. 2. As v_T increases, the $(k, l) \approx (5.8, 5)$ mode becomes more strongly coupled to other modes, following a similar pattern to the ring-beam simulations. Both the ring-beam and shell simulations exhibit a strong nonlinearly driven $(k, l) \approx (8.7, 8)$ mode which does not lie along the magnetoacoustic dispersion branch. Figure 14 shares similar properties with Fig. 11, there is again evidence of mode couplings which are able to produce modes in the high k, and hence high frequency, region. Unlike the ring-beam simulation, no strong modes above the noise level are

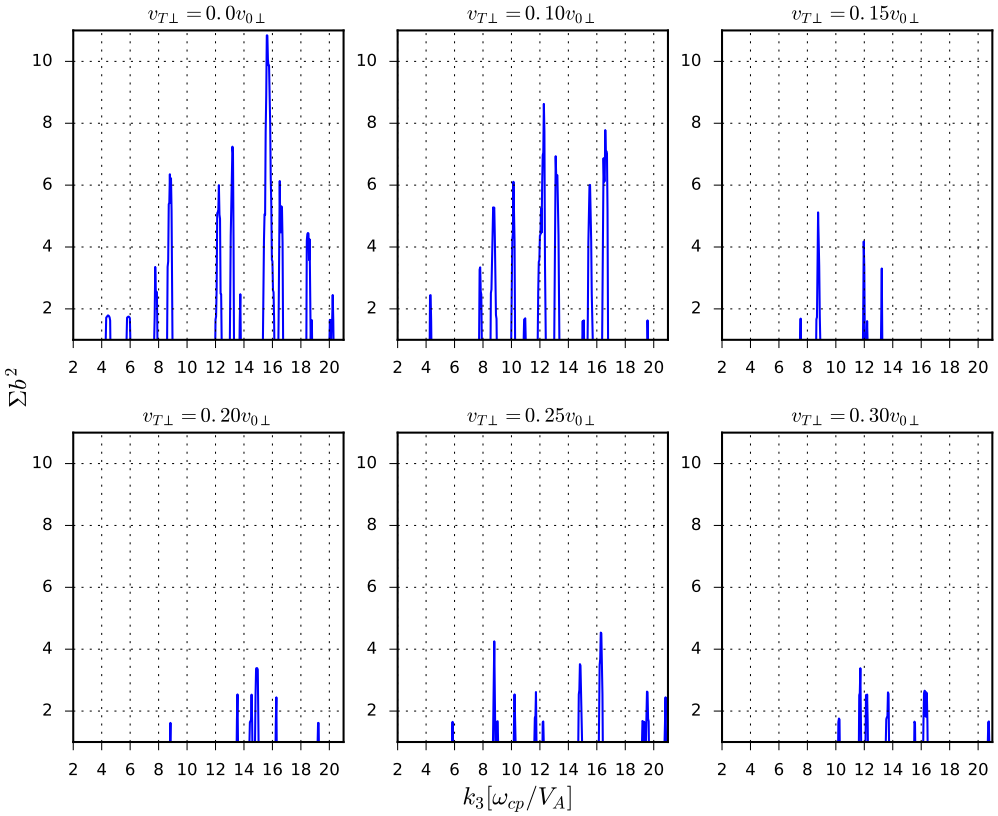

Figure 11: The sum of the square of the bicoherence b_c^2 as a function of normalised wavenumber k_3 from six PIC simulations in which the minority energetic protons are initialised using ring-beam velocity distributions with varying perpendicular velocity spreads. The spread $v_{T\perp}$ as a fraction of the initial perpendicular velocity $v_{0\perp}$ is shown at the top of each panel. The sum is calculated from corresponding data shown in Fig. 10, and $k_3 = k_1 + k_2$ is the child mode resulting from strong linear coupling between two parent modes k_1 and k_2. Only combinations of k_1 and k_2 yielding a value of $b_c^2 \geq 0.8$ (see Fig. 10) are included in the sum. A large value of Σb_c^2 indicates that a child mode in the vicinity of k_3 arises from strong nonlinear coupling between multiple distinct parent modes k_1 and k_2.

observed above the lower hybrid frequency, probably because the intensity of the parent modes is significantly less than that of their ring-beam counterparts.

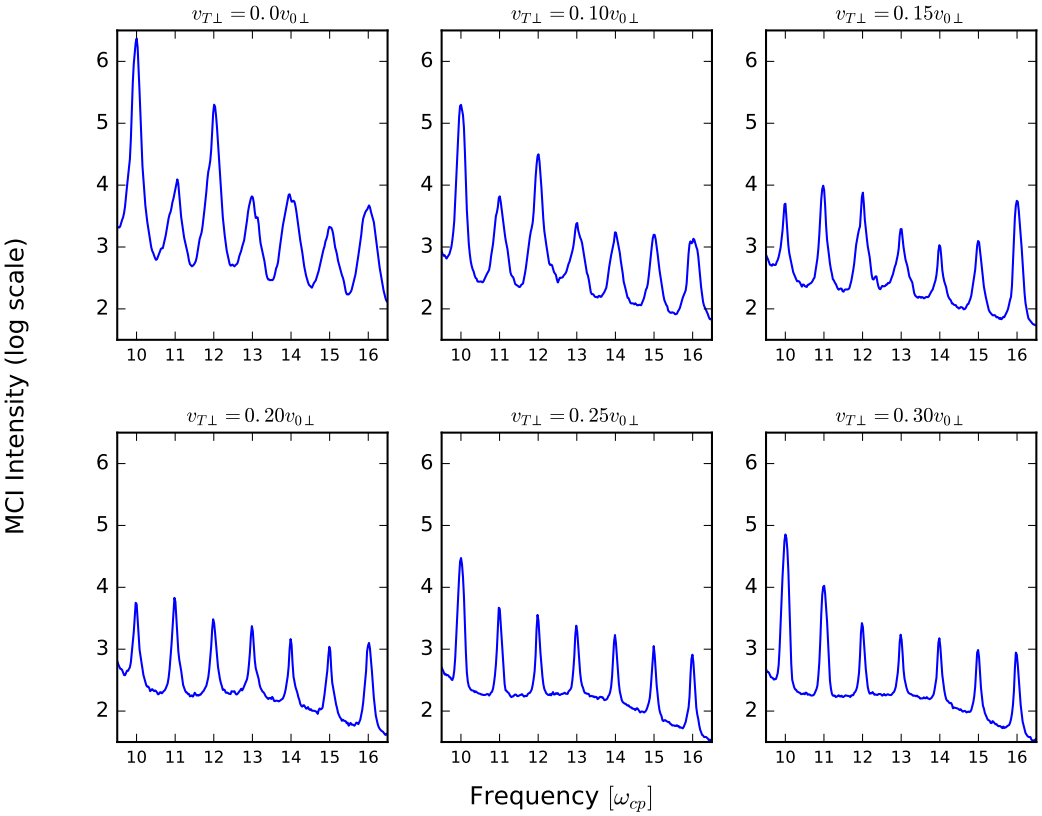

Figure 12: As Fig. 4, except only the region with frequency ω greater than the lower hybrid frequency ω_{LH} is shown. In each panel, the peaks differ in height, suggesting that some of the more intense spectral peaks, e.g. $\omega = 10\omega_{cp}$ in the top left panel, owe their existence to the strong nonlinear wave-wave interactions shown in Figs. 10 and 11. This mode in particular, which is driven entirely by nonlinear wave-wave interactions, has a spectral intensity of comparable magnitude to some of the linearly driven modes shown in Fig. 4. Thus this mode, and others like it in this a priori evanescent region of the frequency domain, have an existential dependence on the minority energetic proton population relaxing under the MCI, which goes beyond that of the linearly excited normal modes of the system that have $\omega < \omega_{LH} \simeq 9\omega_{cp}$.

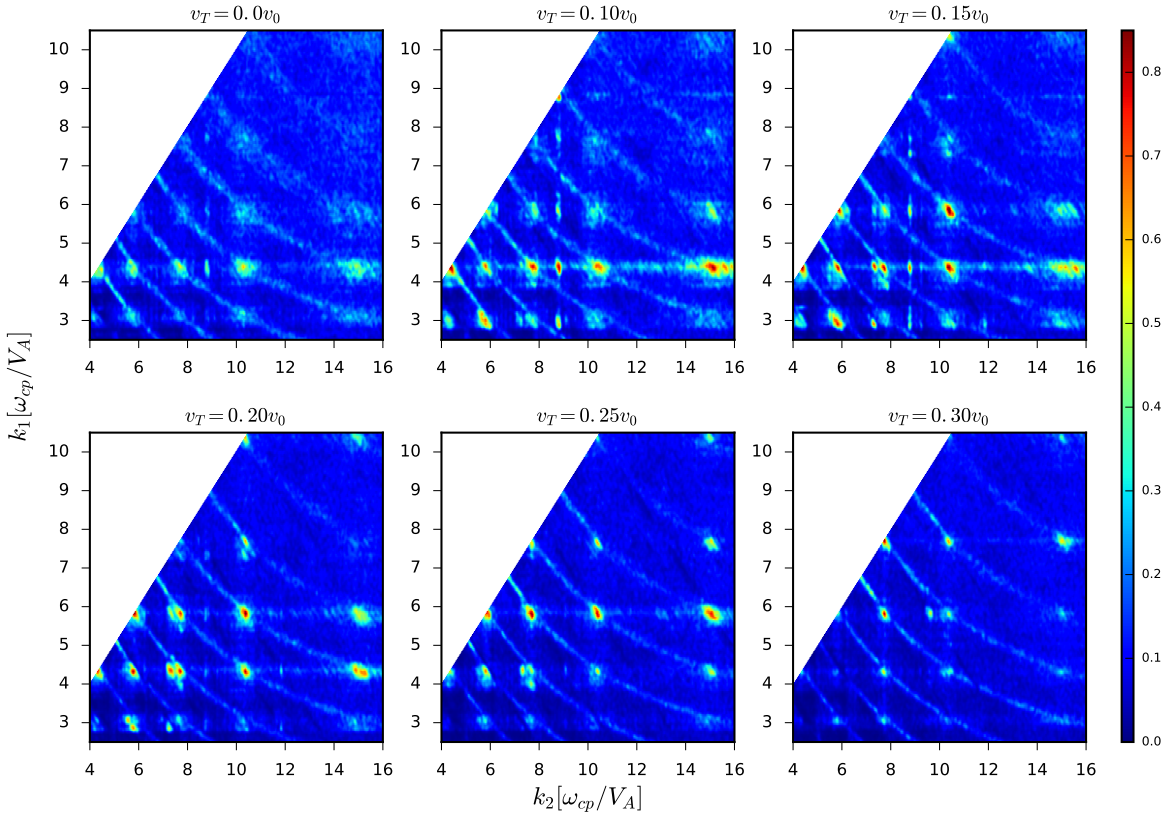

Figure 13: The square of the bicoherence b_c^2 (defined by Eq. D.2) of the oscillatory part of the B_z field component as a function of normalised wavenumber k from six PIC simulations in which the minority energetic protons are initialised using spherical shell velocity distributions with varying velocity spreads. The spread v_T as a fraction of the initial velocity v_0 is shown at the top of each panel. In each plot, b_c^2 is calculated using time series spanning the duration displayed in the corresponding panels shown in Fig. 2. For instance, the bicoherence shown in the top left panel is calculated using time-series up to $t = 73\tau_{cp}$, the bicoherence shown in the top middle is calculated using time-series up to $t = 80\tau_{cp}$, and so on. The minimum significance level is thus $b_c^2 \gtrsim 0.13$. The strength of coupling in the simulation with $v_T = 0$ shown in the top left panel is significantly less than the rest of the simulations.

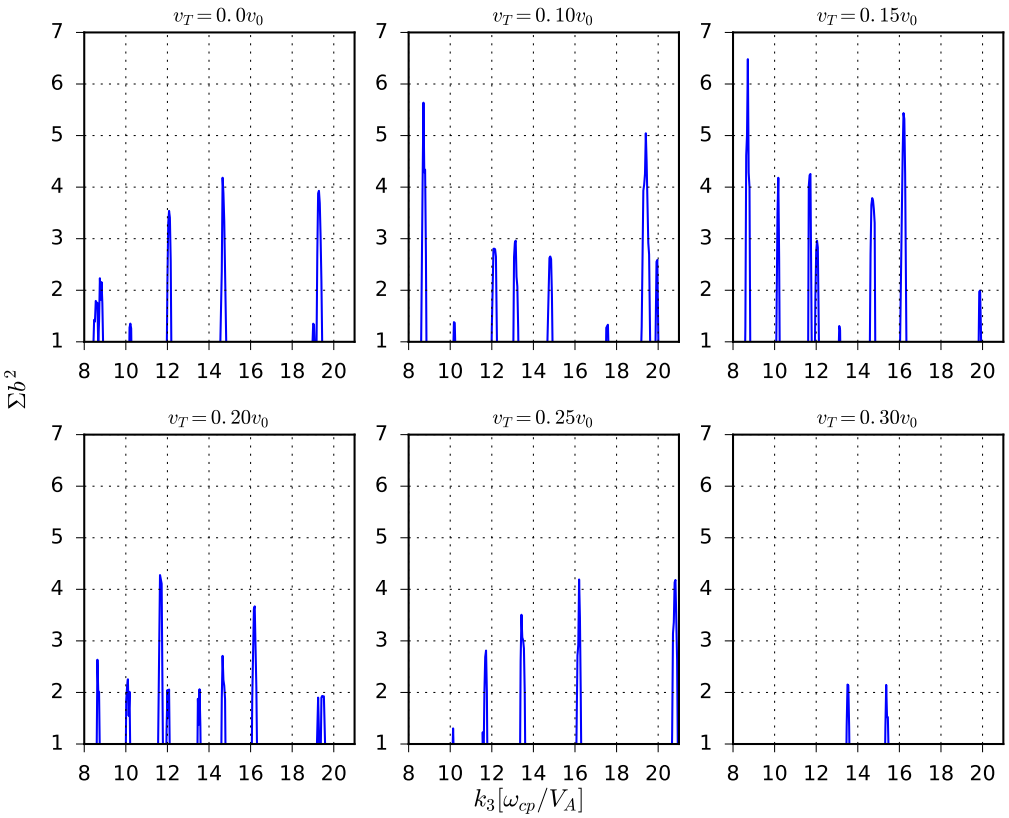

Figure 14: The sum of the square of the bicoherence b^2 as a function of normalised wavenumber k_3 from six PIC simulations in which the minority energetic protons are initialised using spherical shell velocity distributions with varying velocity spreads. The spread v_T as a fraction of the initial perpendicular velocity v_0 is shown at the top of each panel. The sum is calculated from corresponding data shown in Fig. 13, and $k_3 = k_1 + k_2$ is the child mode resulting from strong linear coupling between two parent modes k_1 and k_2. For the upper left panel, which corresponds to a simulation with $v_T = 0.0v_0$, only combinations of k_1 and k_2 yielding a value of $b_c^2 \geq 0.4$ (see Fig. 13) are included in the sum. For the rest of the panels, that is the simulations with finite velocity spread, only combinations of k_1 and k_2 yielding a value of $b_c^2 \geq 0.6$ are included in the sum.

5. Conclusions

Motivated by recent observations of transient ICE from fusion-born ions in the core plasma of AUG [3, 4] and DIII-D [1, 2], we have reported here the first PIC computations of the collective relaxation of a minority energetic proton population represented by an isotropic spherical shell distribution that has finite width in velocity space. These first principles computations self-consistently solve the Maxwell-Lorentz equations for the full gyro-orbit dynamics of kinetic thermal ion, energetic ion, and electron populations. They progress deep into the nonlinear regime of the dominant instability, which is identifiable as the MCI. Fourier transforms of the fields excited in the plasma by the relaxing ions constitute our simulated ICE spectra. This choice of minority ion distribution function is significantly different from the delta-functions used in Refs. [11, 38, 39, 41, 42, 44, 56, 53, 51, 52]. It provides an alternative limit for the model distribution function of fusion-born ions during the onset and early rise of fusion reactivity in the core of future larger tokamak plasmas. Aspects of the resulting MCI physics may be reflected in measurements of ICE from contemporary medium-size tokamak plasmas, where prompt loss plays a substantial role [26, 27, 55], prior to the domination of collisional effects. We have analysed six simulations under these conditions, using a different initial velocity spread in each one, as well as six comparison simulations in which the minority protons were initialised using ring-beam distribution functions with different perpendicular velocity spreads.

We find that the MCI is excited in all cases, and the simulation outcomes reflect the fact that the perpendicular component of energetic ion velocity drives the MCI. A corollary is that energetic ions with high parallel velocities, which are included in the shell, but not in the ring-beam model, are effectively inert. They play a very minor role in the MCI physics of perpendicular propagating waves, while consuming computational resources. Spherical shell simulations take longer to reach MCI saturation than their ring beam counterparts, and give rise to about ten times less energy transfer from the minority ions to the bulk plasma and electromagnetic fields. This reflects the fact that MCI drive is strongest for larger values of $v_\perp/v_A \geq 1$ [44] and the perpendicular component of the minority energetic proton velocity is smaller, on average, in the spherical shell simulations than it is in the ring-beam simulations. The energetic proton populations in both sets of simulations have the same initial total energy. In general, the time to MCI saturation increases with the velocity spread, in both the spherical shell and ring-beam simulations. However, at thermal spreads $v_T \geq 0.2v_0$, the spherical shell simulations exhibit the same linear saturation time of approximately 80 proton gyroperiods. The energy in the excited fields at saturation decreases as the shell spread v_T increases, and the remainder of the free energy in the minority ion distribution is then transferred approximately monotonically to the bulk deuterons.

The spectral structure of the simulated ICE in all PIC computations is qualitatively

similar. The intensity of ICE in the ring-beam simulations is sometimes two orders of magnitude greater than in the spherical shell simulations, owing to the increased energy transfer from the minority protons to the fields. In both cases, increasing the velocity spread leads to the most spectrally intense mode gradually shifting from the fourth proton cyclotron harmonic, to the fifth, and finally to the sixth. This suggests that by observing the mode structure in experiments, one may be able to deduce the spread in velocity space of the minority ion distribution. The early time growth rates of modes in all twelve simulations were found to closely resemble the numerically computed analytical linear growth rates, which were calculated using a first principles kinetic dispersion solver [66].

Nonlinear wave-wave coupling was found to play an important role in determining the spectral structure of the simulated ICE. While there are many more wave-wave interactions in the ring-beam simulations than in the spherical shell simulations, the strongest nonlinearly driven modes of practical interest - i.e., those that contribute significantly to the ICE signal - are present in both sets of simulations. In particular, both sets of simulations exhibit a strong nonlinearly driven $(k, l) \approx (8.7, 8)$ mode which does not lie along the magnetoacoustic dispersion branch, and in the case of the ring-beam simulation with zero velocity spread, contributes to approximately half of the total intensity of the eighth proton cyclotron harmonic. Other nonlinear couplings gave rise to modes above the lower hybrid frequency ω_{LH}, where linear perpendicular-propagating modes are evanescent. In the ring-beam simulations, some of these modes have intensities comparable to low intensity linearly unstable modes. In the $v_{T\perp} = 0.0 v_{0\perp}$ ring-beam simulation, it appears that one of these modes at $(k, l) = (12.2, 10)$ couples to another nonlinearly driven mode at $(k, l) \approx (3.3, 2)$, providing a second source of energy to the eighth proton cyclotron harmonic, which is thus entirely driven by nonlinear interactions. Finally, we identified an instance in which a succession of nonlinear interactions produces a mode which contributes to the secondary drive of the linearly unstable $l = 3$ cyclotron harmonic, whilst being a distinct location in wavevector space. This demonstrates how indispensable the nonlinear physics is, when simulating ICE spectra and interpreting experimental observations. The key to identifying mode couplings is to fulfil the wavenumber matching criterion, followed by the frequency matching criterion. These two requirements suggest that an experimental effort to detect both the perpendicular wavenumber and high frequency ion cyclotron harmonics would improve understanding of the measured ICE frequency spectrum, and hence the character of the energetic ion distribution function which drives it.

The similarities between the outputs of both sets of simulations, shell and ring-beam, are substantial. These include: the dependence of time-evolving energy densities on velocity spread; the linearly excited mode structure; and the nonlinear phenomena. We infer that a ring-beam velocity distribution for the minority energetic ions serves as a close approximation to an isotropic spherical shell distribution, provided that the

velocity spread is not too large. From a resource perspective this is crucial. Both sets of simulations reported here used large numbers of computational particles and ran for a long time, in order to generate high quality spectra. The ring-beam simulations reported here are around half as computationally demanding as their spherical shell counterparts, because they take half as long to reach linear saturation. Furthermore, the intensity of the ICE harmonic peaks in the ring-beam simulations is much higher than in the spherical shell simulations. We conclude that in future simulations for core ICE interpretation, ring-beam distributions may provide an acceptable proxy for shell distributions, while using significantly fewer computational particles and still maintaining a satisfactory signal-to-noise ratio. The diagnostics with which to measure core ICE in tokamaks are becoming more widespread, and the computing resources with which to simulate it are becoming increasingly sophisticated. It will soon be feasible for PIC simulations of the MCI to provide a new level of interpretation capability for the characteristics of energetic ion velocity distributions in relation to measured ICE spectra. The relatively inexpensive ring-beam simulations offer a way to realise this, in contexts where a shell distribution may actually be more realistic.

Acknowledgments

This project used the EPOCH code, part funded by UK EPSRC grants EP/G054950/1, EP/G056803/1, EP/G055165/1 and EP/ M022463/1. This work was carried out within the framework of the EUROfusion Consortium and has received funding from the Euratom research and training programme 2014-2018 and 2019-2020 under grant agreement No 633053. The work received support from the RCUK Energy Programme grant no. EP/P012450/1. The views and opinions expressed herein do not necessarily reflect those of the European Commission. S.C.C acknowledges a Fulbright-Lloyd's of London Scholarship and AFOSR grant FA9550-17-1-0054.

Appendix A. Particle-in-cell approach

Particle-in-cell (PIC) codes [78] self-consistently evolve the relativistic full gyro-orbit dynamics of very large numbers of charged particles, together with the spatially and temporally evolving self-consistent electric and magnetic fields, which are governed by the full set of Maxewell's equations. Coupling between particles and fields occurs through the relativistic Lorentz force law, Gauss' law, and Maxwell's generalisation of Ampère's law. The full system of equations solved by the PIC code is

$$\nabla \times \mathbf{E} = -\frac{\partial \mathbf{B}}{\partial t}, \tag{A.1}$$

$$\nabla \times \mathbf{B} = \mu_0 \left(\mathbf{J} + \epsilon_0 \frac{\partial \mathbf{E}}{\partial t} \right), \tag{A.2}$$

$$\frac{d\mathbf{p}_i}{dt} = q_i \left(\mathbf{E} + \mathbf{v}_i \times \mathbf{B} \right). \tag{A.3}$$

Here $\mathbf{E}, \mathbf{B}$, and $\mathbf{J}$ are the electric field, magnetic field, and current density; ρ is the charge density; and $\mathbf{v}_i, \mathbf{p}_i$, and q_i denote the velocity and momentum vectors and charge of the ith particle in the simulation. The electric and magnetic fields are evolved on a grid using a finite difference scheme, and the "Boris" [78] scheme is used to evolve the relativistic particle trajectories. The current density in Eq. A.2 is obtained by using the Esirkepov generalisation of the Villasenor and Buneman scheme [79, 80]. The advantage of this scheme is that both Gauss's law and the no monopoles condition are automatically satisfied. In the work presented in this paper we use the EPOCH [40] PIC code. This is second order accurate, relativistically correct, and fully MPI parallelised. EPOCH has been successfully applied to a range of magnetic confinement fusion (MCF) relevant plasma physics problems [41, 51, 52, 39, 53, 81, 82, 83, 84, 85, 86].

Appendix B. Finding roots of the kinetic linear dispersion relation using a numerical approach

The linear dispersive properties of electric and magnetic waves in plasma may be computed by solving the wave equation:

$$\frac{c^2}{\omega^2}\left(\mathbf{k}\otimes\mathbf{k} - k^2\mathbf{1}\right) + \boldsymbol{\epsilon} = \mathbf{0}, \tag{B.1}$$

where $\mathbf{k}\otimes\mathbf{k}$ denotes the outer product between two wavevectors, ω is the frequency of the wave and $\mathbf{1}$ is the unit dyadic. Following Stix [87], in the non-relativistic regime the dielectric tensor for a gyrotropic homogeneous magnetized plasma is given by

$$\boldsymbol{\epsilon} = \mathbf{1} + \sum_s \frac{\omega_{ps}^2}{\omega\Omega_{cs}} \sum_{n=-\infty}^{\infty} \int_{-\infty}^{\infty}\int_{0}^{\infty} \frac{2\pi\Omega_{cs} v_\perp dv_\perp dv_\parallel}{\omega - k_\parallel v_\parallel - n\Omega_{cs}} \mathbf{S}_n, \tag{B.2}$$

where Ω_{cs} is the cyclotron frequency, and ω_{ps} is the plasma frequency of charged particle species s. The tensor component is described by the definitions:

$$\mathbf{S}_n = \begin{bmatrix} n^2 J_n^2 v_\perp U/z^2 & inJ_nJ_n' v_\perp U/z & nJ_n^2 v_\perp U/z \\ -inJ_nJ_n' v_\perp U/z & (J_n')^2 v_\perp U & -iJ_nJ_n' v_\parallel U \\ nJ_n^2 v_\perp U/z & iJ_nJ_n' v_\parallel U & J_n^2 v_\parallel W \end{bmatrix}, \tag{B.3}$$

$$U = \frac{\partial f}{\partial v_\perp} + \frac{k_\parallel}{\omega}\left(v_\perp \frac{\partial f}{\partial v_\parallel} - v_\parallel \frac{\partial f}{\partial v_\perp}\right), \tag{B.4}$$

$$W = \left(1 - \frac{n\Omega_{cs}}{\omega}\right)\frac{\partial f}{\partial v_\parallel} + \frac{n\Omega_{cs} v_\parallel}{\omega v_\perp}\frac{\partial f}{\partial v_\perp}. \tag{B.5}$$

Here, J_n denotes the nth Bessel function of the first kind, J_n' denotes its derivative, and both take the argument $z = k_\perp v_\perp/\Omega_{cs}$. Equation B.1 may then be solved to calculate the dispersion relation between the complex frequency and wavevector for given multi-species particle distribution functions $f_s(v_\parallel, v_\perp)$.

In this manuscript we have used a numerical root finding code to compute the kinetic dispersion relation [66, 67], allowing us to efficiently calculate the linear growth rates of the MCI. This code efficiently solves Eq. B.1 for ω by computing the integrals in Eq. B.2, for an arbitrary number of plasma species, each represented by arbitrary gyrotropic particle distributions sampled on Cartesian grids. In the results presented in this manuscript, the thermal plasma species were represented by Maxwellian distribution functions, while the minority energetic ions were represented using either a ring-beam or spherical shell distribution function. Roots of Eq. B.1 are obtained convergently using the Nelder-Mead simplex method for gradient descent, and by repeatedly evaluating the determinant of the matrix defined by the left hand side of this equation. Similar methodology has previously been used by Hellinger et al. to study the oblique electron firehose instability [88], and similar non-relativistic [89] and fully relativistic [90] dispersion relation solving codes have recently been published.

Appendix C. Solutions of the 1993 analytical linear theory

Figure C1 shows the analytical linear growth rates γ of the MCI (see Eq. 31 of Ref. [27]) due to the relaxation of minority energetic protons represented using a spherical shell distribution. The trend of decreasing γ with increasing v_T is consistent with the lower panels of Fig. 7; however, the peak growth rate is located at higher harmonic number. This is because, in order to remain within the limits of analytical tractability, Eq. 31 of Ref. [27] approximates the MCI dispersion relation as $\omega \approx k_\perp v_A$; which is no longer valid as $\omega \to \omega_{LH}$. Growth rates for distributions with $v_T > 0.235$ are zero, and are not shown here. There is a discontinuity in the analytical expression at $v_T = 0$, so instead we calculate the growth rates for $v_T = 0.01 v_0$.

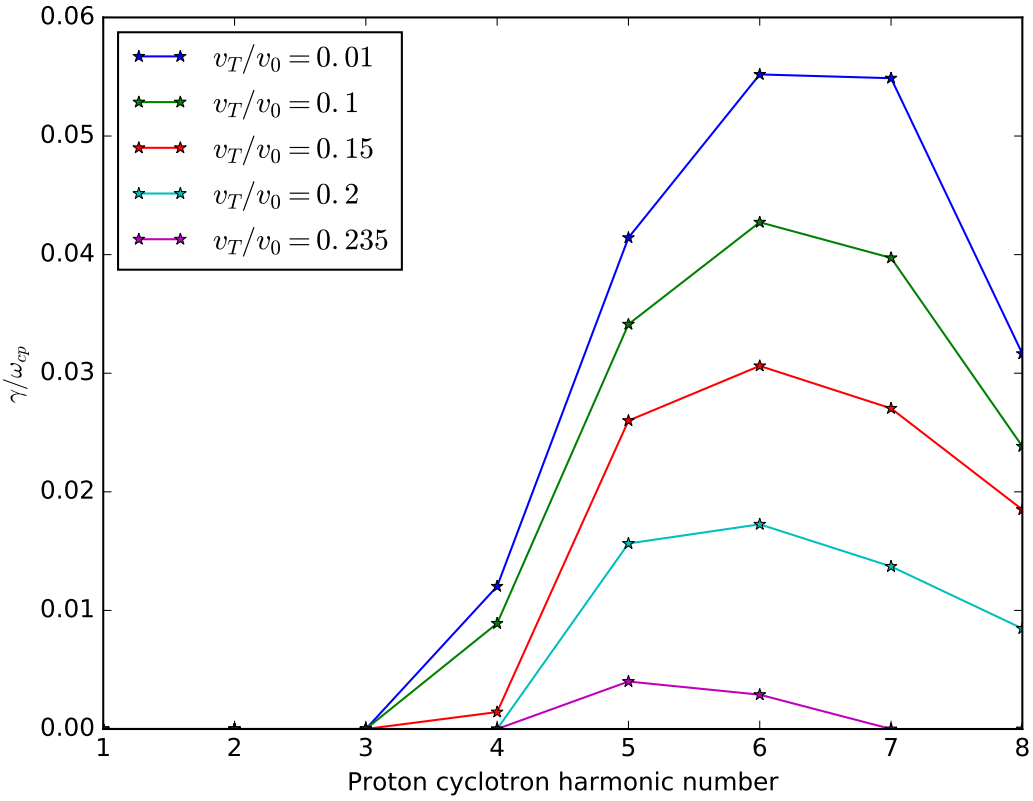

Figure C1: Contour plot displaying the linear growth rates of the MCI as a function of velocity spread v_T and proton cyclotron harmonic number. The minority protons are represented using a spherical shell distribution and the growth rate, calculated according to Eq. 31 of Ref. [27], is normalised to the proton cyclotron frequency ω_{cp}. This analytically calculated growth rate is maximum around the sixth proton cyclotron harmonic and decreases as the shell thickness increases. Comparator plots are in the bottom pair of panels of Fig. 7, for numerical root-finder (left) and direct PIC simulations (right).

Appendix D. Bispectrum and bicoherence

There is extensive literature which describes higher order spectral techniques including bispectral analysis. For general information we refer to Refs. [68, 69, 71, 72]; and for plasma-specific applications, for example, Refs. [73, 74, 75, 50, 72]. An early account of the application of higher order spectral techniques to plasma physics is given in Ref. [70].

Any three waves interacting nonlinearly must satisfy, to good approximation, the frequency and wavenumber matching conditions:

$$f_3 = f_1 + f_2 \qquad \boldsymbol{k_3} = \boldsymbol{k_1} + \boldsymbol{k_2}.$$

To measure the amount of phase coherence between three modes that obey the above resonance conditions, one can compute the bispectrum as follows. Defining $F(f_1)$ as the complex Fourier transform of a quantity (for instance an electromagnetic field component) at frequency $f = f_1$, and $F^*(f_1)$ as its conjugate, the bispectrum is defined as:

$$b_s^2\left(f_1, f_2\right) = \mid \left\langle F\left(f_1\right) F\left(f_2\right) F^*\left(f_1 + f_2\right)\right\rangle \mid^2, \tag{D.1}$$

where the brackets $\langle\cdot\rangle$ denote averaging over time.

One can normalise the bispectrum to obtain the bicoherence. This can be done in several ways [68, 91], one of which is to use Schwartz's inequality:

$$b_c^2\left(f_1, f_2\right) = \frac{\mid \left\langle F\left(f_1\right) F\left(f_2\right) F^*\left(f_1 + f_2\right)\right\rangle \mid^2}{\left\langle \mid F\left(f_1\right) F\left(f_2\right) \mid^2\right\rangle \left\langle \mid F^*\left(f_1 + f_2\right) \mid^2\right\rangle}, \tag{D.2}$$

which ensures $b_c^2 \leq 1$. Thus the bicoherence is a measure of the intrinsic strength of wave-wave coupling, whereas the bispectrum measures the operational strength of nonlinear coupling given the wave amplitudes. The number of *independent* Fourier transforms M, must be large enough so that the value of the bicoherence b_c is statistically significant. For significant coupling the variance of b_c^2 is given by [70]

$$Var\left(b_c^2\right) \simeq \frac{b_c^2}{M}\left(1 - b_c^2\right). \tag{D.3}$$

Therefore if $b_c > 1/\sqrt{M}$, we have a statistically significant result. All bicoherence dependant conclusions in this manuscript satisfy this condition.

References

[1] Thome K E, Pace D C, Pinsker R I, Meneghini O, del Castillo C A and Zhu Y 2018 *Review of Scientific Instruments* **89** 10I102 URL https://doi.org/10.1063/1.5035561

[2] Thome K E, Pace D C, Pinsker R I, Zeeland M A V, Heidbrink W W and Austin M E 2019 *Nuclear Fusion* URL http://iopscience.iop.org/10.1088/1741-4326/ab20e7

[3] Ochoukov R, Bobkov V, Chapman B, Dendy R O, Dunne M, Faugel H, Garca-Muoz M, Geiger B, Hennequin P, McClements K G, Moseev D, Nielsen S, Rasmussen J, Schneider P, Weiland M and Noterdaeme J M 2018 *Review of Scientific Instruments* **89** 10J101 URL https://doi.org/10.1063/1.5035180

[4] Ochoukov R, Bilato R, Bobkov V, Chapman B, Chapman S, Dendy R, Dunne M, Faugel H, Garca-Muoz M, Geiger B, Kallenbach A, Kappatou A, McClements K, Moseev D, Nielsen S, Rasmussen J, Schneider P, Weiland M, Noterdaeme J M, Team A U and Team E M 2019 *Nuclear Fusion* **59** 014001 URL http://stacks.iop.org/0029-5515/59/i=1/a=014001

[5] D'Inca R 2014 *Ion Cyclotron Emission on ASDEX Upgrade* Ph.D. thesis Ludwig-Maximilians-Universitat

[6] Cottrell G A and Dendy R O 1988 *Phys. Rev. Lett.* **60**(1) 33–36 URL https://link.aps.org/doi/10.1103/PhysRevLett.60.33

[7] Cottrell G, Bhatnagar V, Costa O D, Dendy R, Jacquinot J, McClements K, McCune D, Nave M, Smeulders P and Start D 1993 *Nuclear Fusion* **33** 1365 URL http://stacks.iop.org/0029-5515/33/i=9/a=I10

[8] Schild P, Cottrell G and Dendy R 1989 *Nuclear Fusion* **29** 834 URL http://stacks.iop.org/0029-5515/29/i=5/a=013

[9] Cottrell G A 2000 *Phys. Rev. Lett.* **84**(11) 2397–2400 URL https://0-link-aps-org.pugwash.lib.warwick.ac.uk/doi/10.1103/PhysRevLett.84.2397

[10] Jacquet P, BergerBy G, Bobkov V, Blackman T, Day I E, Durodi F, Graham M, Hellsten T, Laxback M, Mayoral M, Monakhov I, Nightingale M, Sharapov S E, Vrancken M and contributors J E 2011 *AIP Conference Proceedings* **1406** 17–20 URL https://aip.scitation.org/doi/abs/10.1063/1.3664919

[11] McClements K, Brisset A, Chapman B, Chapman S, Dendy R, Jacquet P, Kiptily V, Mantsinen M, Reman B and Contributors J 2018 *Nuclear Fusion* **58** 096020 URL http://stacks.iop.org/0029-5515/58/i=9/a=096020

[12] Cauffman S, Majeski R, McClements K and Dendy R 1995 *Nuclear Fusion* **35** 1597 URL http://stacks.iop.org/0029-5515/35/i=12/a=I22

[13] Heidbrink W W, Austin M E, Fisher R K, García-Munoz M, Matsunaga G, McKee G R, Moyer R A, Muscatello C M, Okabayashi M, Pace D C, Shinohara K, Solomon W M, Strait E J, Zeeland M A V and Zhu Y B 2011 *Plasma Physics and Controlled Fusion* **53** 085028 URL http://stacks.iop.org/0741-3335/53/i=8/a=085028

[14] Kimura H, Kusama Y, Saigusa M, Kramer G, Tobita K, Nemoto M, Kondoh T, Nishitani T, Costa O D, Ozeki T, Oikawa T, Moriyama S, Morioka A, Fu G, Cheng C and Afanas'ev V 1998 *Nuclear Fusion* **38** 1303 URL http://stacks.iop.org/0029-5515/38/i=9/a=304

[15] Ichimura M, Higaki H, Kakimoto S, Yamaguchi Y, Nemoto K, Katano M, Ishikawa M, Moriyama S and Suzuki T 2008 *Nuclear Fusion* **48** 035012 URL http://stacks.iop.org/0029-5515/48/i=3/a=035012

[16] Sato S, Ichimura M, Yamaguchi Y, Katano M, Imai Y, Murakami T, Miyake Y, Yokoyama T, Moriyama S, Kobayashi T, Kojima A, Shinohara K, Sakamoto Y, Watanabe T, Hojo H and Imai T 2010 *Plasma and Fusion Research* **5** S2067

[17] Liu L N, Zhang X J, Zhu Y B, Qin C M, Zhao Y P, Yuan S, Mao Y Z, Li M H, Chen Y, Cheng J, Ping L L, Li H and Ai L 2019 *Review of Scientific Instruments* **90** 063504 URL https://doi.org/10.1063/1.5089537

[18] Kim M, Thatipamula S, Lee J, Choi M, Park H, Akiyama T and Yun G 2018 *Nuclear Fusion* **58**

096034 URL http://stacks.iop.org/0029-5515/58/i=9/a=096034

[19] Thatipamula S G, Yun G S, Leem J, Park H K, Kim K W, Akiyama T and Lee S G 2016 *Plasma Physics and Controlled Fusion* **58** 065003 URL http://stacks.iop.org/0741-3335/58/i=6/a=065003

[20] Saito K, Kasahara H, Seki T, Kumazawa R, Mutoh T, Watanabe T, Shimpo F, Nomura G, Osakabe M, Ichimura M, Higaki H and Komori A 2009 *Fusion Engineering and Design* **84** 1676 – 1679 ISSN 0920-3796 proceeding of the 25th Symposium on Fusion Technology URL http://www.sciencedirect.com/science/article/pii/S0920379608005073

[21] Saito K, Kumazawa R, Seki T, Kasahara H, Nomura G, Shimpo F, Igami H, Isobe M, Ogawa K, Toi K, Osakabe M, Nishiura M, Watanabe T, Yamamoto S, Ichimura M, Mutoh T and Group L E 2013 *Plasma Science and Technology* **15** 209 URL http://stacks.iop.org/1009-0630/15/i=3/a=03

[22] Shalashov A, V Suvorov E, V Lubyako L, Maassberg H and Team t 2003 *Plasma Physics and Controlled Fusion* **45** 395

[23] McClements K, D'Inca R, Dendy R, Carbajal L, Chapman S, Cook J, Harvey R, Heidbrink W and Pinches S 2015 *Nuclear Fusion* **55** 043013 URL http://stacks.iop.org/0029-5515/55/i=4/a=043013

[24] Dendy R O and McClements K G 2015 *Plasma Physics and Controlled Fusion* **57** 044002 URL http://stacks.iop.org/0741-3335/57/i=4/a=044002

[25] Belikov V S and Kolesnichenko Y I 1976 *Sov. Phys. Tech. Phys.* **20** 1146

[26] Dendy R O, LashmoreDavies C N and Kam K F 1992 *Physics of Fluids B: Plasma Physics* **4** 3996–4006 (*Preprint* https://doi.org/10.1063/1.860304) URL https://doi.org/10.1063/1.860304

[27] Dendy R O, LashmoreDavies C N and Kam K F 1993 *Physics of Fluids B: Plasma Physics* **5** 1937–1944 (*Preprint* https://doi.org/10.1063/1.860781) URL https://doi.org/10.1063/1.860781

[28] Dendy R O, LashmoreDavies C N, McClements K G and Cottrell G A 1994 *Physics of Plasmas* **1** 1918–1928 (*Preprint* https://doi.org/10.1063/1.870647) URL https://doi.org/10.1063/1.870647

[29] Dendy R O, McClements K G, LashmoreDavies C N, Majeski R and Cauffman S 1994 *Physics of Plasmas* **1** 3407–3413 URL https://doi.org/10.1063/1.870489

[30] Dendy R, McClements K, Lashmore-Davies C, Cottrell G, Majeski R and Cauffman S 1995 *Nuclear Fusion* **35** 1733 URL http://stacks.iop.org/0029-5515/35/i=12/a=I38

[31] McClements K G, Dendy R O, LashmoreDavies C N, Cottrell G A, Cauffman S and Majeski R 1996 *Physics of Plasmas* **3** 543–553 (*Preprint* https://doi.org/10.1063/1.871881) URL https://doi.org/10.1063/1.871881

[32] McClements K G, Hunt C, Dendy R O and Cottrell G A 1999 *Phys. Rev. Lett.* **82**(10) 2099–2102 URL https://link.aps.org/doi/10.1103/PhysRevLett.82.2099

[33] Fülöp T, Kolesnichenko Y, Lisak M and Anderson D 1997 *Nuclear Fusion* **37** 1281 URL http://stacks.iop.org/0029-5515/37/i=9/a=I08

[34] Fülöp T and Lisak M 1998 *Nuclear Fusion* **38** 761 URL http://stacks.iop.org/0029-5515/38/i=5/a=309

[35] Fülöp T, Lisak M, Kolesnichenko Y I and Anderson D 2000 *Physics of Plasmas* **7** 1479–1486 (*Preprint* https://doi.org/10.1063/1.873967) URL https://doi.org/10.1063/1.873967

[36] Sumida S, Shinohara K, Ikezoe R, Ichimura M, Sakamoto M, Hirata M and Ide S 2017 *Journal of the Physical Society of Japan* **86** 124501 (*Preprint* https://doi.org/10.7566/JPSJ.86.124501) URL https://doi.org/10.7566/JPSJ.86.124501

[37] Sumida S, Shinohara K, Ikezoe R, Ichimura M, Sakamoto M, Hirata M and Ide S 2018 *Plasma Physics and Controlled Fusion* URL http://iopscience.iop.org/10.1088/1361-6587/aaf184

[38] Carbajal L, Dendy R O, Chapman S C and Cook J W S 2014 *Physics of Plasmas* **21** 012106 URL

https://doi.org/10.1063/1.4861866
[39] Chapman B, Dendy R O, Chapman S C, McClements K G, Yun G S, Thatipamula S G and Kim M 2019 *Nuclear Fusion* URL https://doi.org/10.1088%2F1741-4326%2Fab35a7
[40] Arber T D, Bennett K, Brady C S, Lawrence-Douglas A, Ramsay M G, Sircombe N J, Gillies P, Evans R G, Schmitz H, Bell A R and Ridgers C P 2015 *Plasma Physics and Controlled Fusion* **57** 1–26
[41] Cook J W S, Dendy R O and Chapman S C 2013 *Plasma Physics and Controlled Fusion* **55** 065003 URL http://stacks.iop.org/0741-3335/55/i=6/a=065003
[42] Carbajal L, Dendy R O, Chapman S C and Cook J W S 2017 *Phys. Rev. Lett.* **118**(10) 105001 URL https://link.aps.org/doi/10.1103/PhysRevLett.118.105001
[43] Reman B C G, Dendy R O, Akiyama T, Chapman S C, Cook J W S, Igami H, Inagaki S, Saito K and Yun G S 2016 *EPS Conference Proceedings* **P2.041** URL http://epsppd.epfl.ch/Madeira/html/authors/nav/AutT02fr.html
[44] Reman B, Dendy R, Akiyama T, Chapman S, Cook J, Igami H, Inagaki S, Saito K and Yun G 2019 *Nuclear Fusion* **59** 096013 URL https://doi.org/10.1088%2F1741-4326%2Fab2ca2
[45] Kirk A, Koch B, Scannell R, Wilson H R, Counsell G, Dowling J, Herrmann A, Martin R and Walsh M (the MAST team) 2006 *Phys. Rev. Lett.* **96**(18) 185001 URL https://0-link-aps-org.pugwash.lib.warwick.ac.uk/doi/10.1103/PhysRevLett.96.185001
[46] Leonard A W 2014 *Physics of Plasmas* **21** 090501 URL https://doi.org/10.1063/1.4894742
[47] Kamiya K, Asakura N, Boedo J, Eich T, Federici G, Fenstermacher M, Finken K, Herrmann A, Terry J, kirk A, Koch B, Loarte A, Maingi R, Maqueda R, Nardon E, Oyama N and Sartori R 2007 *Plasma Physics and Controlled Fusion* **49** S43 URL http://stacks.iop.org/0741-3335/49/i=7/a=S03
[48] Loarte A, Saibene G, Sartori R, Campbell D, Becoulet M, Horton L, Eich T, Herrmann A, Matthews G, Asakura N, Chankin A, Leonard A, Porter G, Federici G, Janeschitz G, Shimada M and Sugihara M 2003 *Plasma Physics and Controlled Fusion* **45** 1549 URL http://stacks.iop.org/0741-3335/45/i=9/a=302
[49] Zohm H 1996 *Plasma Physics and Controlled Fusion* **38** 105 URL http://stacks.iop.org/0741-3335/38/i=2/a=001
[50] Lee J, Yun G S, Choi M J, Kwon J M, Jeon Y M, Lee W, Luhmann N C and Park H K 2016 *Phys. Rev. Lett.* **117**(7) 075001 URL https://link.aps.org/doi/10.1103/PhysRevLett.117.075001
[51] Chapman B, Dendy R, McClements K, Chapman S, Yun G, Thatipamula S and Kim M 2017 *Nuclear Fusion* **57** 124004 URL http://stacks.iop.org/0029-5515/57/i=12/a=124004
[52] Chapman B, Dendy R, Chapman S, McClements K, Yun G, Thatipamula S and Kim M 2018 *Nuclear Fusion* **58** 096027 URL http://stacks.iop.org/0029-5515/58/i=9/a=096027
[53] Cook J W S, Dendy R O and Chapman S C 2017 *Phys. Rev. Lett.* **118**(18) 185001 URL https://link.aps.org/doi/10.1103/PhysRevLett.118.185001
[54] Thomas P, Giroud C, Lomas P, Stubberfield P, Sharapov S, Testa D and Team D E 2001 *EPS Conference Proceedings* **P3.001** URL http://ocs.ciemat.es/EPS2016PAP/pdf/P2.041.pdf
[55] D J S 1979 *Proceedings of the Varenna Course on Physics of Plasmas Close to Thermonuclear Conditions* vol I (Varenna, Commission of the European Communities, Brussels)
[56] Reman B C G, Dendy R O, Akiyama T, Chapman S C, Cook J W S, Igami H, Inagaki S, Saito K and Yun G S 2019 *Nuclear Fusion* **XX** XXXXX URL XXXX
[57] Kolesnichenko Y, Fülöp T, Lisak M and Anderson D 1998 *Nuclear Fusion* **38** 1871 URL http://stacks.iop.org/0029-5515/38/i=12/a=311
[58] Kolesnichenko Y, Lisak M and Anderson D 2000 *Nuclear Fusion* **40** 1419 URL http://stacks.iop.org/0029-5515/40/i=7/a=311
[59] Smith H, Fülöp T, Lisak M and Anderson D 2003 *Physics of Plasmas* **10** 1437–1442 URL https://doi.org/10.1063/1.1566441
[60] Hellsten T and Laxback M 2003 *Physics of Plasmas* **10** 4371–4377 URL https://doi.org/10.

1063/1.1617315
[61] Hellsten T, Holmström K, Johnson T, Bergkvist T and Laxback M 2006 *Nuclear Fusion* **46** S442 URL http://stacks.iop.org/0029-5515/46/i=7/a=S07
[62] Smith H M and Verwichte E 2009 *Plasma Physics and Controlled Fusion* **51** 075001 URL http://stacks.iop.org/0741-3335/51/i=7/a=075001
[63] Gorelenkov N N and Cheng C Z 1995 *Physics of Plasmas* **2** 1961–1971 (*Preprint* https://doi.org/10.1063/1.871281) URL https://doi.org/10.1063/1.871281
[64] Gorelenkov N N 2016 *Plasma Physics Reports* **42** 430–439 ISSN 1562-6938 URL https://doi.org/10.1134/S1063780X16050044
[65] R O Dendy B Chapman J W S C and Reman B C G 2019 *Abstract submitted to the 61st Annual Meeting of the APS Division of Plasma Physics, Fort Lauderdale, Florida, October 21-25* **Log DPP19-2019-000031**
[66] Irvine S A 2018 *Collective Instability and Physics of the Anomalous Doppler Resonance in Fusion Plasmas* Ph.D. thesis The University of Warwick
[67] Irvine S 2019 *GitHub repository* URL https://github.com/samuelirvine/Kinetic-Dispersion-Solver
[68] de Witt T D 2003 *Numerical Schemes for the Analysis of Turbulence - A Tutorial (Space Plasma Simulation, Lecture Notes in Physics, vol 615) ed J. Büchner, M. Scholer, and C. T. Dum* (Berlin: Springer)
[69] Kim Y C, Beall J M, Powers E J and Miksad R W 1980 *The Physics of Fluids* **23** 258–263 URL https://aip.scitation.org/doi/abs/10.1063/1.862966
[70] Kim Y C and Powers E J 1979 *IEEE Transactions on Plasma Science* **7** 120–131 ISSN 0093-3813
[71] Kaup D J, Reiman A and Bers A 1979 *Rev. Mod. Phys.* **51**(2) 275–309 URL https://0-link-aps-org.pugwash.lib.warwick.ac.uk/doi/10.1103/RevModPhys.51.275
[72] Itoh S I, Itoh K, Nagashima Y and Kosuga Y 2017 *Plasma and Fusion Research* **12** 1101003
[73] Holland C, Tynan G R, Diamond P H, Moyer R A and Burin M J 2002 *Plasma Physics and Controlled Fusion* **44** A453 URL http://stacks.iop.org/0741-3335/44/i=5A/a=350
[74] Moyer R A, Tynan G R, Holland C and Burin M J 2001 *Phys. Rev. Lett.* **87**(13) 135001 URL https://link.aps.org/doi/10.1103/PhysRevLett.87.135001
[75] Yamada T, Itoh S I, Maruta T, Kasuya N, Nagashima Y, Shinohara S, Terasaka K, Yagi M, Inagaki S, Kawai Y, Fujisawa A and Itoh K 2008 *Nature Physics* **4** 721–725
[76] Cairns R A 1985 *Plasma Physics* (Dordrecht: Kluwer Academic Publishers Group) pp 62–92
[77] Verdon A L, Cairns I H, Melrose D B and Robinson P A 2009 *Physics of Plasmas* **16** 052105 (*Preprint* https://doi.org/10.1063/1.3132628) URL https://doi.org/10.1063/1.3132628
[78] Birdsall C K and Langdon A B 1985 *Plasma Physics Via Computer* (New York, NY, USA: McGraw-Hill, Inc.) ISBN 0070053715
[79] Esirkepov T 2001 *Computer Physics Communications* **135** 144 – 153 ISSN 0010-4655 URL http://www.sciencedirect.com/science/article/pii/S0010465500002289
[80] Villasenor J and Buneman O 1992 *Computer Physics Communications* **69** 306–316
[81] Cook J W S, Chapman S C, Dendy R O and Brady C S 2011 *Plasma Physics and Controlled Fusion* **53** 065006 URL http://stacks.iop.org/0741-3335/53/i=6/a=065006
[82] Cook J W S, Dendy R O and Chapman S C 2011 *Plasma Physics and Controlled Fusion* **53** 074019 URL http://stacks.iop.org/0741-3335/53/i=7/a=074019
[83] Cook J W S, Chapman S C and Dendy R O 2010 *Phys. Rev. Lett.* **105**(25) 255003 URL https://link.aps.org/doi/10.1103/PhysRevLett.105.255003
[84] Gingell P W, Chapman S C, Dendy R O and Brady C S 2012 *Plasma Physics and Controlled Fusion* **54** 065005 URL http://stacks.iop.org/0741-3335/54/i=6/a=065005
[85] Gingell P W, Chapman S C and Dendy R O 2013 *Plasma Physics and Controlled Fusion* **55** 055010 URL http://stacks.iop.org/0741-3335/55/i=5/a=055010
[86] Gingell P W, Chapman S C and Dendy R O 2014 *Plasma Physics and Controlled Fusion* **56**

035012 URL http://stacks.iop.org/0741-3335/56/i=3/a=035012
[87] Stix T H 1992 *Waves in Plasmas* (American Institute of Physics) ISBN 0883188597
[88] Hellinger P, Trvnek P M, Decyk V K and Schriver D 2014 *Journal of Geophysical Research: Space Physics* **119** 59–68 (*Preprint* https://agupubs.onlinelibrary.wiley.com/doi/pdf/10.1002/2013JA019227) URL https://agupubs.onlinelibrary.wiley.com/doi/abs/10.1002/2013JA019227
[89] Astfalk P and Jenko F 2016 *Journal of Geophysical Research: Space Physics* **122** 89–101 (*Preprint* https://agupubs.onlinelibrary.wiley.com/doi/pdf/10.1002/2016JA023522) URL https://agupubs.onlinelibrary.wiley.com/doi/abs/10.1002/2016JA023522
[90] Verscharen D, Klein K, D G Chandran B, Stevens M, S Salem C and D Bale S 2018 *Journal of Plasma Physics* **84**
[91] Kravtchenko-Berejnoi V, Lefeuvre F, Krasnossel'skikh V and Lagoutte D 1995 *Signal Processing* **42** 291 – 309 ISSN 0165-1684 URL http://www.sciencedirect.com/science/article/pii/016516849400136N